Sanz, MA.; Nguyen, K.; Latorre, M.; Rodríguez, M.; Montáns, FJ. (2019). Sheet metal forming analysis using a large strain anisotropic multiplicative plasticity formulation, based on elastic correctors, which preserves the structure of the infinitesimal theory. Finite Elements in Analysis and Design. 164:1-17. https://doi.org/10.1016/j.finel.2019.06.004

Sheet metal forming analysis using a large strain anisotropic multiplicative plasticity formulation, based on elastic correctors, which preserves the structure of the infinitesimal theory

Miguel A. Sanz[a,*], K. Nguyen[a], Marcos Latorre[b], Manuel Rodríguez[a], Francisco J. Montáns[a]

[a] *Escuela Técnica Superior de Ingeniería Aeronáutica y del Espacio, Universidad Politécnica de Madrid, Pza. Cardenal Cisneros, 28040, Madrid, Spain*

[b] *Department of Biomedical Engineering, Yale University, New Heaven, USA*

Abstract

Sheet metal forming is a very important process in industry to create a wide variety of goods. The analysis of local ductility and residual stresses is important both to assess the viability of the manufacturing process and the reliability of the resulting elements in service. An example is crash-worthiness, where remaining ductility and residual stresses govern the safety of the overall structure during the impact.

A main ingredient of finite element simulations for sheet metal forming in industry is a robust continuum-based computational algorithm for large strain elastoplasticity which includes both elastic and plastic anisotropy, as well as mixed hardening. The theory should use exactly-integrable (conservative) elastic and hardening behaviors based on physically motivated proper state variables and, if possible, result in a simple integration algorithm. In this work we implement a novel large strain formulation for anisotropic hyperelasto-plasticity in a user subroutine of the commercial program ADINA to perform sheet metal forming simulations, testing the robustness and suitability of the model for industry, as well as its accuracy. The formulation is based on a new approach to the treatment of large strain kinematics, using logarithmic elastic corrector rates instead of plastic rates. Furthermore, kinematic hardening is formulated without an explicit backstress. We compare and discuss the results with those in the literature which use alternative frameworks.

Keywords: Large strains; anisotropic plasticity; sheet metal forming; logarithmic strains; multiplicative decomposition; Hill plasticity.

1. Introduction

The manufacturing process of metal goods, such as automobiles, typically employ sheet metal forming procedures which entail large displacements, contacts and large deformations

*Corresponding author

Email addresses: miguelangel.sanz@upm.es (Miguel A. Sanz), khanhnguyen.gia@upm.es (K. Nguyen), marcos.latorre@yale.edu (Marcos Latorre), (Manuel Rodríguez), fco.montans@upm.es (Francisco J. Montáns)

[1]. Due to manufacturing processes like rolling, metal sheets are anisotropic [2]. Metal forming procedures are complex, and the resulting product may need to sustain important loads and/or is involved in safety parts of a structure, like in crash-worthiness. Therefore, the analysis of residual stresses [3], and of the remaining ductility [4], are important in many applications [5, 6, 7].

Efficient finite element simulations which use large strain continuum plasticity models are now systematically employed in analysing the deformation processes involved [8]. However, several issues may affect the reliability of the obtained solutions if the computational algorithm is affected by lack of objectivity, shear stress oscillation, spurious elastic dissipation, or the lack of weak-invariance under reference configuration changes [9]. Hence, sound large strain integration algorithms for plasticity are pursued for general applications, and in particular, for metal forming applications. To have the desired generality, these large strain algorithms should be valid for anisotropic elasticity, anisotropic plasticity and mixed hardening, including the possibility of incorporating nonlinear kinematic hardening and viscoelastic effects in a simple manner. Furthermore, simplicity and robustness of the stress integration algorithm are also important assets [8, 10].

Traditionally, continuum formulations and their related stress integration algorithms were based on objective stress rates [11] and incrementally objective algorithms, as the Hughes-Winget [12] and Rolph-Bathe [13] algorithms. Probably, because there were no simple alternatives to treat flow kinematics, these algorithms are still used in commercial codes, especially for anisotropic materials. However, hypoelastic-based formulations may present shear stress oscillation and spurious elastic dissipation [14, 15] because, except in the case of using the logarithmic rate and linear elasticity [16], they fail to fulfill Bernstein's integrability conditions [17, 18]. Because of this, Simo and co-workers popularized the use of hyperelastic formulations in the context of large strain elastoplasticity [19, 20]. The elastic state variable for hyperelasticity can be obtained either from additive Green ansatzes and plastic metrics (e.g. [21, 22, 23, 24, 25, 26], among many others) or from Kröner-Lee multiplicative decompositions (e.g. [19, 27, 28, 29], among others). The former misses a clear microstructural motivation and has been recently criticised for loosing ellipticity properties during plastic flow [30], and for lacking weak-invariance [9] (i.e. results depend on the arbitrary reference configuration).

When using multiplicative decompositions, there are mainly two approaches. The first one, due to Simo, which allowed arbitrary isotropic stored energies [11], is the use of quadratic measures and of a flow rule in terms of the Lie derivative of the elastic left Cauchy-Green (or the Finger) strain tensor [31, 32], resulting in an *unconventional* [33] flow rule of arguably difficult interpretation, which initially failed to preserve volume during plastic flow, an issue solved in subsequent works [34, 33]. The second approach, due to Eterović and Bathe [35] and Weber and Anand [36], is the use of logarithmic strains and an exponential mapping. This approach resulted in very attractive additive integration algorithms similar to the small strain ones, in which large strain kinematics were taken into account just with explicit pre- and post-processors, a remarkable simple framework emphasized by the work of Eterovic and Bathe [35]. Because of the attractive simple implementation, this approach was followed later by other researchers which developed formulations in spatial configuration and/or used principal deformations [33, 37]. However, in contrast to the latter spatial for-

mulations, even though it is seldom recognized, the algorithm of Eterović and Bathe allows for anisotropic yield functions and kinematic hardening; but elasticity is linear in logarithmic strains, further restricted to isotropy and to moderate strains, and kinematic hardening must be linear. Hence, formulations without those restrictions have been pursued for long time. For example, Caminero et al [29] removed the restriction of elastic isotropy for the Eterović and Bathe algorithm, keeping the additive, small strain structure. In a similar way, Papadopoulus and Lu [24] and Miehe et al [23] used plastic metrics instead of the multiplicative decomposition to obtain additive ansatzes in anisotropic elastoplasticity. More recently, using the alternative pulled-back formulation within the context of the multiplicative decomposition (see for example Remark 9.2.1 in [11]), Vladimirov et al [27, 28] used a lagrangian approach taking advantage of some properties of the right Cauchy-Green strain tensors and using the exponential mapping to preserve volume. However, this approach results in a more complex formulation loosing the appealing structure of the infinitesimal framework. Similar formulations include[38, 39, 40, 41, 42, 43, 44], among others. Badreddine et al [45] proposed a formulation that preserves the structure of the small strain theory by assuming the elastic strain to be small compared to plastic strain in order to get additive decomposition of the total strain rate tensor. A recent comparison of different approaches may be found in [46]. Additive Green approaches are still a common selection for complex materials, see for example the recent work [47].

Obviously, sheet metal forming simulations need efficient and robust algorithms which account for both elastic and plastic anisotropy, and which also allow for nonlinear mixed hardening. Kinematic hardening is of energetic nature (non-disipative) so it requires a proper state variable tensor to enter the stored energy terms. This stored energy term gives a proper definition of the backstress and guarantees stable cycles in the case of kinematic hardening; see [48, 49]. Usually, the chosen state variable is either the plastic Cauchy-Green strain tensor or an *energetic* deformation obtained from the (subsequent) Lion multiplicative decomposition of the *plastic* deformation gradient. Unfortunately, these approaches become computationally more complicated with nonlinear kinematic hardening, where further nested decompositions are needed.

A solution to most of the difficulties found in the large strain kinematics when using hyperelasticity and Kröner-Lee multiplicative decompositions was found in [50] using elastic correctors directly derived from the chain rule and *conventional* flow rules in terms of these strains. The framework is in line with anisotropic large strain nonequilibrium viscoelasticity [51, 52] and the theory replicates the typical scheme of the closest-point projection algorithms, *but also at the continuum level* so the algorithm results in a plain backward-Euler implementation of the continuum theory. As a result, the iterative part of the plastic stress integration algorithm is identical to the small strains one, being additive, simple and volume-preserving [53] *by construction*. For the case of isotropic elastoplasticity, we have shown that an efficient algorithm is possible reproducing the case of nonlinear kinematic hardening with multiple backstresses following the Armstrong-Frederick rule [54], noteworthy without even explicitly employing the backstress concept. Large strain kinematics are in our formulations reduced to geometric, noniterative (explicit), pre- and post-processors. Continuum and algorithmic constitutive tangents in the intermediate configuration are also identical to small strains ones, but in terms of logarithmic strains and their work-conjugate generalized Kirchhoff stresses. A

relevant drawback of other formulations including anisotropic elasticity is the presence of the non-symmetric Mandel stresses in the formulation and the coupling of the plastic spin with the symmetric flow, so alternatives are desired, see e.g. [55]. Remarkably, these drawbacks are not present in our formulation.

However, a successful elastoplasticity formulation should not only be shown to be satisfying on theoretical grounds and to be numerically simple and efficient, but it should also clearly prove to be useful for industry, being capable to rival established formulations in meaningful simulations in commercial software. As aforementioned, sheet metal forming simulations are very demanding and important for industry, so a large number of publications are dedicated to prove the usefulness of proposed formulations and their algorithmic implementations to sheet metal forming; e.g. [48, 56, 57, 58, 59, 60, 61, 62], among many others. Therefore, the purpose of the present work is to show that a simple implementation of anisotropic multiplicative hyperelasto-plasticity including mixed hardening is possible, showing furthermore the robustness and applicability of the novel framework to simulate several complex sheet metal forming benchmarks. To validate the formulation for these types of simulations, we compare the results obtained with our flow rule in terms of elastic correctors with other formulations which use flow rules in terms of plastic rates.

To this end, in the next section we describe the formulation used in this paper, which was programmed as a user subroutine in the commercial finite element program ADINA. Thereafter, we demonstrate the applicability of the approach to different sheet metal forming problems and perform the comparison with established formulations. Because the algorithm and the prescription of material parameters is very simple, similar to the small strains case (because it is formulated in logarithmic strains), we also discuss several aspects on their influence in the results.

2. Anisotropic finite elastoplasticity model

In this section we derive the most important aspects of the continuum formulation and stress integration algorithm used in this work.

2.1. Continuum formulation

The material model is motivated from the rheological model for the small strain formulation as shown in Fig. 1, which includes an "*internal*" Prandtl (friction-spring) element in parallel with an "*external*"single Hooke (spring) element. This Hooke element is responsible for the phenomenologically observable (macroscopic) kinematic hardening of the model. The approach differs from the classical kinematic hardening which assumes explicitly a backstress and its evolution. In the context of *isotropic* elastoplasticity, the behavior typical of the Chaboche and Ohno-Wang models based on the Armstrong-Frederick rule can be obtained using a Besseling structure with multiple Prandtl devices, avoiding the assumption of backstresses and the use of the Lion decomposition [54]. Furthermore, it is noted that either a linear or a nonlinear hyperelastic relation between the strain and stress tensor can be assigned to the Hooke element, resulting in a kinematic hardening which is also linear or nonlinear in terms of the corresponding conjugate pair of strain and stress measures. Noteworthy, at large strains, a linear kinematic hardening in terms of logarithmic strains and generalized

Kirchhoff stresses may be nonlinear in terms of other strain and stress measures as shown in Ref. [53].

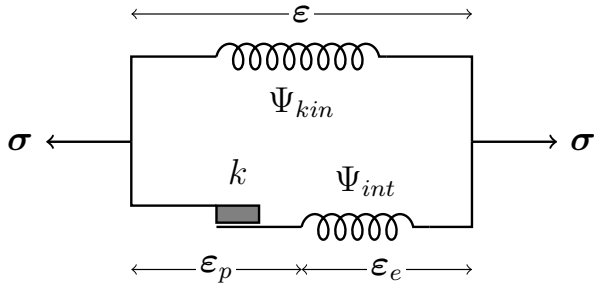

Figure 1: Proposed rheological model motivating the anisotropic finite elastoplasticity model with combined isotropic and kinematic nonlinear hardening

For obtaining the proper elastic state variables entering the stored energy terms, the Kröner-Lee multiplicative decomposition of the deformation gradient $\boldsymbol{F}$ into an elastic part $\boldsymbol{F}_e$ and a plastic part $\boldsymbol{F}_p$ is employed

$$\boldsymbol{F} = \boldsymbol{F}_e \boldsymbol{F}_p \tag{1}$$

Consider the internal elastic Green-Lagrange strains in the intermediate configuration $\boldsymbol{A}_e := \frac{1}{2}(\boldsymbol{F}_e^T \boldsymbol{F}_e - \boldsymbol{I})$ as a function of the total independent external Green-Lagrange strains $\boldsymbol{A} := \frac{1}{2}(\boldsymbol{F}^T \boldsymbol{F} - \boldsymbol{I})$ and the independent internal plastic deformation gradient $\boldsymbol{F}_p$—note that we use the symbol $\boldsymbol{A}$ for Green-Lagrange strains to reserve $\boldsymbol{E}$ for material logarithmic strains

$$\boldsymbol{A}_e(\boldsymbol{A}, \boldsymbol{A}_p) = \boldsymbol{F}_p^{-T}(\boldsymbol{A} - \boldsymbol{A}_p)\boldsymbol{F}_p^{-1} = \boldsymbol{F}_p^{-T} \odot \boldsymbol{F}_p^{-T} : (\boldsymbol{A} - \boldsymbol{A}_p) \tag{2}$$

in which the operator $\odot$ is the mix dyadic product between two second order tensors defined as $(\boldsymbol{Y} \odot \boldsymbol{Z})_{ijkl} = Y_{ik} Z_{jl}$. This expression shows that $\boldsymbol{A}_e, \boldsymbol{A}, \boldsymbol{A}_p$ are not additive because $\boldsymbol{A}_e$ lives in a different configuration from that of $\boldsymbol{A}$ and $\boldsymbol{A}_p$. If $\boldsymbol{A} - \boldsymbol{A}_p$ is pushed forward to the intermediate configuration, we obtain $\boldsymbol{A}_e$. However, because of their salient features [63], we are interested in using the natural logarithmic strain framework. Since the one-to-one relations $\boldsymbol{E}_e = \boldsymbol{E}_e(\boldsymbol{A}_e)$, $\boldsymbol{A}_p(\boldsymbol{F}_p)$ and $\boldsymbol{E} = \boldsymbol{E}(\boldsymbol{A})$ hold, where $\boldsymbol{E}_e = \frac{1}{2}\ln(\boldsymbol{F}_e^T \boldsymbol{F}_e)$ and $\boldsymbol{E} = \frac{1}{2}\ln(\boldsymbol{F}^T \boldsymbol{F})$ are the elastic and total material logarithmic strain tensors in their respective configurations, we can obtain also the general dependence $\boldsymbol{E}_e(\boldsymbol{E}, \boldsymbol{F}_p)$ and hence, we can decompose the elastic logarithmic strain-rate tensor into the addition of two partial contributions:

$$\dot{\boldsymbol{E}}_e = \left.\frac{\partial \boldsymbol{E}_e}{\partial \boldsymbol{E}}\right|_{\dot{\boldsymbol{F}}_p = \boldsymbol{0}} : \dot{\boldsymbol{E}} + \left.\frac{\partial \boldsymbol{E}_e}{\partial \boldsymbol{F}_p}\right|_{\dot{\boldsymbol{E}} = \boldsymbol{0}} : \dot{\boldsymbol{F}}_p = \dot{\boldsymbol{E}}_e|_{\dot{\boldsymbol{F}}_p = \boldsymbol{0}} + \dot{\boldsymbol{E}}_e|_{\dot{\boldsymbol{E}} = \boldsymbol{0}} \tag{3}$$

The first addend is obtained when the (internal) dissipative evolution is frozen, whereas the second addend is obtained when the external power is frozen, and only internal evolution is allowed. Using the operator split usually employed in computational inelasticity within the algorithmic framework, we can interpret these terms as follows

$$\dot{\boldsymbol{E}}_e = \dot{\boldsymbol{E}}_e|_{\dot{\boldsymbol{F}}_p = \boldsymbol{0}} + \dot{\boldsymbol{E}}_e|_{\dot{\boldsymbol{E}} = \boldsymbol{0}} = {}^{tr}\dot{\boldsymbol{E}}_e + {}^{ct}\dot{\boldsymbol{E}}_e \tag{4}$$

where ${}^{tr}\dot{\boldsymbol{E}}_e$ is the trial elastic contribution to the rate of the total elastic logarithmic strain $\dot{\boldsymbol{E}}_e$, and depends on the total logarithmic strain rate $\dot{\boldsymbol{E}}$ only (i.e. the plastic evolution given by $\boldsymbol{F}_p$ is frozen). The rate ${}^{ct}\dot{\boldsymbol{E}}_e$ is the plastic corrector contribution to the total elastic logarithmic strain rate $\dot{\boldsymbol{E}}_e$ and depends on the total plastic deformation gradient rate $\dot{\boldsymbol{F}}_p$ only (i.e. the external deformation given by $\boldsymbol{E}$ is frozen).

The stored energy function may be expressed in terms of any Lagrangian strain measure, or associated invariants. Herein, it is written in terms of the total and elastic logarithmic strains and decomposes additively into two parts: $\Psi_{kin}(\boldsymbol{E})$, the strain energy function associated with the "*external*" spring element, and $\Psi_{int}(\boldsymbol{E}_e)$, the strain energy function associated with the "*internal*" spring element as in the rheological model. Then, we write

$$\Psi(\boldsymbol{E},\boldsymbol{E}_e) = \Psi_{kin}(\boldsymbol{E}) + \Psi_{int}(\boldsymbol{E}_e) \tag{5}$$

By using work-conjugacy (see details in [50]), the stress power per reference volume may be written in terms of $\boldsymbol{E}$ and its work-conjugate in the most general case, the material "*generalized*" Kirchhoff stress tensor $\boldsymbol{T}$, as

$$\mathcal{P} = \boldsymbol{S} : \dot{\boldsymbol{A}} = \boldsymbol{T} : \dot{\boldsymbol{E}} \tag{6}$$

where $\boldsymbol{S}$ is the second Piola-Kirchhoff stress tensor in the reference configuration. Note also that all quantities in this equation are in the reference configuration. In the typical tests performed in principal material axes under proportional loading the stresses $\boldsymbol{T}$ are coincident with the spatial Kirchhoff stresses, so the identification of material constants is very simple.

According to the Clausius-Duhem inequality for the iso-thermal processes, the dissipation written in terms of Lagrangian logarithmic strains can be determined as

$$\mathcal{D}^P = \mathcal{P} - \dot{\Psi} = \mathcal{P} - \dot{\Psi}_{kin} - \dot{\Psi}_{int} = \boldsymbol{T} : \dot{\boldsymbol{E}} - \boldsymbol{T}_{kin} : \dot{\boldsymbol{E}} - \boldsymbol{T}^{|e}_{int} : \dot{\boldsymbol{E}}_e \tag{7}$$

where we defined

$$\boldsymbol{T}_{kin} = \frac{d\Psi_{kin}(\boldsymbol{E})}{d\boldsymbol{E}} \quad \text{and} \quad \boldsymbol{T}^{|e}_{int} = \frac{d\Psi_{int}(\boldsymbol{E}_e)}{d\boldsymbol{E}_e} \tag{8}$$

Note that $\boldsymbol{T}_{kin}$, as $\boldsymbol{E}$, lives in the reference configuration and $\boldsymbol{T}^{|e}_{int}$, as $\boldsymbol{E}_e$, lives in the intermediate configuration.

Consider that dissipation is frozen, so $\dot{\boldsymbol{F}}_p = \boldsymbol{0}$ and therefore we have $\dot{\boldsymbol{E}}_e \equiv {}^{tr}\dot{\boldsymbol{E}}_e = \partial \boldsymbol{E}_e/\partial \boldsymbol{E}|_{\dot{\boldsymbol{F}}_p=\boldsymbol{0}} : \dot{\boldsymbol{E}}$, in this case, the dissipation inequality is

$$\mathcal{D}^P = \left(\boldsymbol{T} - \boldsymbol{T}_{kin} - \boldsymbol{T}^{|e}_{int} : \left.\frac{\partial \boldsymbol{E}_e}{\partial \boldsymbol{E}}\right|_{\dot{\boldsymbol{F}}_p=\boldsymbol{0}} \right) : \dot{\boldsymbol{E}} = 0 \quad \text{if} \quad \dot{\boldsymbol{F}}_p = \boldsymbol{0} \tag{9}$$

Since the strain rate may take arbitrary values, Eq. (9) requires in general that

$$\boldsymbol{T} = \boldsymbol{T}_{kin} + \boldsymbol{T}^{|e}_{int} : \left.\frac{\partial \boldsymbol{E}_e}{\partial \boldsymbol{E}}\right|_{\dot{\boldsymbol{F}}_p=\boldsymbol{0}} = \boldsymbol{T}_{kin} + \boldsymbol{T}_{int} \tag{10}$$

in which (note the abuse of notation in using the same symbol for the energy when considering different arguments; we make explicit the dependencies when needed)

$$\boldsymbol{T}_{int} = \frac{d\Psi_{int}(\boldsymbol{E}_e)}{d\boldsymbol{E}_e} : \left.\frac{\partial \boldsymbol{E}_e}{\partial \boldsymbol{E}}\right|_{\dot{\boldsymbol{F}}_p=\boldsymbol{0}} = \boldsymbol{T}^{|e}_{int} : \left.\frac{\partial \boldsymbol{E}_e}{\partial \boldsymbol{E}}\right|_{\dot{\boldsymbol{F}}_p=\boldsymbol{0}} \equiv \left.\frac{\partial \Psi_{int}(\boldsymbol{E},\boldsymbol{F}_p)}{\partial \boldsymbol{E}}\right|_{\dot{\boldsymbol{F}}_p=\boldsymbol{0}} \tag{11}$$

Note that the tensor $\partial \boldsymbol{E}_e/\partial \boldsymbol{E}|_{\dot{\boldsymbol{F}}_p=\boldsymbol{0}}$ is physically a geometric mapping tensor which performs a pull-back of $\boldsymbol{T}^{|e}_{int}$ from the intermediate configuration (where it lives with $\boldsymbol{E}_e$) to the material one (where $\boldsymbol{E}$ lives). If we now freeze the external power, so $\dot{\boldsymbol{E}} = \boldsymbol{0}$ (i.e. the external deformation given by $\boldsymbol{E}$ is frozen and there is a plastic evolution $\dot{\boldsymbol{F}}_p \neq \boldsymbol{0}$), we get $\dot{\boldsymbol{E}}_e = {}^{ct}\dot{\boldsymbol{E}}_e = \partial \boldsymbol{E}_e/\partial \boldsymbol{F}_p|_{\dot{\boldsymbol{E}}=\boldsymbol{0}} : \dot{\boldsymbol{F}}_p$, the dissipation inequality of Eq. (7) is

$$\mathcal{D}^P \equiv -\left.\dot{\Psi}_{int}\right|_{\dot{\boldsymbol{E}}=\boldsymbol{0}} = -\boldsymbol{T}^{|e}_{int} : {}^{ct}\dot{\boldsymbol{E}}_e > 0 \quad \text{if} \quad \dot{\boldsymbol{F}}_p \neq \boldsymbol{0} \tag{12}$$

Remarkably, it is expressed in terms of purely *symmetric* tensors of elastic nature lying in the intermediate configuration, namely the corrector contribution to the elastic logarithmic strain rate $\dot{\boldsymbol{E}}_e$ and its power-conjugate generalized Kirchhoff stress tensor $\boldsymbol{T}^{|e}_{int} = d\Psi_{int}/d\boldsymbol{E}_e$. The dissipation inequality obtained in Eq. (12) should be positive for all possible motions according to the second law of thermodynamics, which imposes the restrictions on the possible forms of the plastic evolution. Herein, we consider that the plastic evolution is given by the maximum plastic dissipation, i.e. an associative flow rule is adopted as follows:

$${}^{ct}\dot{\boldsymbol{E}}_e = -\dot{\Gamma}\nabla\phi_T = -\dot{\gamma}\frac{1}{\frac{2}{3}k}\nabla\phi_T = -\dot{\gamma}\frac{1}{\frac{2}{3}k}\mathbb{N}_T : \boldsymbol{T}^{|e}_{int} \tag{13}$$

where $\dot{\gamma} = \frac{2}{3}k\dot{\Gamma} \geq 0$ is the plastic consistency parameter (equivalent plastic strain rate), power-conjugate of the reference yield stress parameter k. The scalar function $\phi_T(\boldsymbol{T}^{|e}_{int})$ is the Lagrangian internal convex potential so $\nabla\phi_T := d\phi_T/d\boldsymbol{T}^{|e}_{int}$ is the flow direction, which we take as $\nabla\phi_T = \mathbb{N}_T : \boldsymbol{T}^{|e}_{int}$ and $\mathbb{N}_T$ is a positive-definite fully symmetric fourth order tensor of yield constants associated with the preferred material axes in the intermediate configuration. This tensor $\mathbb{N}_T$ may be deviatoric as in Hill's yield function or could include volumetric terms for pressure-sensitive plasticity. With this consideration, the dissipation inequality in Eq. (12) can be written as

$$\mathcal{D}^P = \dot{\gamma}\frac{1}{\frac{2}{3}k}\boldsymbol{T}^{|e}_{int} : \mathbb{N}_T : \boldsymbol{T}^{|e}_{int} > 0 \quad \text{if} \quad \dot{\gamma} > 0 \tag{14}$$

Alternatively, giving the physical meaning of dissipation to $k\dot{\gamma}$,

$$\mathcal{D}^P = \dot{\gamma}\frac{1}{\frac{2}{3}k}\left(\boldsymbol{T}^{|e}_{int} : \mathbb{N}_T : \boldsymbol{T}^{|e}_{int} - \tfrac{2}{3}k^2\right) + k\dot{\gamma} \equiv k\dot{\gamma} > 0 \quad \text{if} \quad \dot{\gamma} > 0 \tag{15}$$

where the yield function $f_T(\boldsymbol{T}^{|e}_{int}, k)$ can be identified as a function of the elastic generalized Kirchhoff stress tensor and the plastic loading condition in the intermediate configuration:

$$f_T(\boldsymbol{T}^{|e}_{int}, k) = \boldsymbol{T}^{|e}_{int} : \mathbb{N}_T : \boldsymbol{T}^{|e}_{int} - \tfrac{2}{3}k^2 = 0 \quad \text{if} \quad \dot{\gamma} > 0 \tag{16}$$

and the loading/unloading condition also can be identified as

$$\dot{\gamma} = 0 \quad \text{if} \quad f_T(\boldsymbol{T}^{|e}_{int}, k) = \boldsymbol{T}^{|e}_{int} : \mathbb{N}_T : \boldsymbol{T}^{|e}_{int} - \tfrac{2}{3}k^2 < 0 \tag{17}$$

in such a way that the dissipation inequality is finally given in terms of the internal flow stress $k > 0$ and its power-conjugate slip rate $\dot{\gamma} > 0$ through $\mathcal{D}^P = k\dot{\gamma} \geq 0$. From Eq. (10), the total stresses $\boldsymbol{T}$ include two contributions, one from the external kinematic hardening stresses $\boldsymbol{T}_{kin}$, and one from the internal isotropic stresses $\boldsymbol{T}_{int}$. In rate form, we have the following relation:

$$\begin{aligned} \dot{\boldsymbol{T}} &= \dot{\boldsymbol{T}}_{kin} + \dot{\boldsymbol{T}}_{int} = \mathbb{A}_{kin} : \dot{\boldsymbol{E}} + \mathbb{A}_{int} : \dot{\boldsymbol{E}} \\ &= (\underbrace{\mathbb{A}_{kin} + \mathbb{A}_{int}}_{\mathbb{A}}) : \dot{\boldsymbol{E}} = \mathbb{A} : \dot{\boldsymbol{E}} \end{aligned} \tag{18}$$

where $\mathbb{A}_{kin}$ are the external kinematic moduli, $\mathbb{A}_{int}$ are the internal elastoplastic tangent moduli and $\mathbb{A}$ are the continuum tangent moduli of the model. All moduli are written in the reference configuration. Of course, we could interpret $\boldsymbol{T}_{kin}$ as a sort of backstress, so $\dot{\boldsymbol{T}}_{int} = \dot{\boldsymbol{T}} - \dot{\boldsymbol{T}}_{kin}$, but note that $\boldsymbol{T}_{int}$ is not the quantity naturally used in the yield criterion (it is $\boldsymbol{T}^{|e}_{int}$ instead). Hence, the explicit assumption of the backstress brings difficulties in the kinematics which are not present in our formulation, where all these stresses are derived from stored energy terms in the proper configurations.

The stresses $\boldsymbol{T}_{kin}$ depend only on the "external" logarithmic strain tensor $\boldsymbol{E}$ and are determined from the strain energy function $\Psi_{kin}(\boldsymbol{E})$ once the logarithmic strains $\boldsymbol{E}$ are obtained from the deformation gradient $\boldsymbol{F}$. Hence, the linearization of $\boldsymbol{T}_{kin}(\boldsymbol{E})$ in the reference configuration is trivial and the external moduli can be determined from the hyperelastic relation

$$\mathbb{A}_{kin} := \frac{d\boldsymbol{T}_{kin}}{d\boldsymbol{E}} = \frac{d^2\Psi_{kin}(\boldsymbol{E})}{d\boldsymbol{E}d\boldsymbol{E}} \tag{19}$$

As mentioned previously, the stresses tensor $\boldsymbol{T}_{int}$ represents the pull-back operation of $\boldsymbol{T}^{|e}_{int}$ from the intermediate configuration to the reference configuration. Therefore, in order to determine the internal elastoplastic tangent moduli $\mathbb{A}_{int}$ in the reference configuration, we have to determine the internal elastoplastic tangent moduli in the intermediate configuration where plastic flow takes place. The rate of the internal stresses tensor $\boldsymbol{T}^{|e}_{int}$ in the intermediate configuration can be determined as:

$$\dot{\boldsymbol{T}}^{|e}_{int} = \frac{d\boldsymbol{T}_{int}}{d\boldsymbol{E}_e} : \dot{\boldsymbol{E}}_e = \mathbb{A}^{|e}_{int} : \dot{\boldsymbol{E}}_e \tag{20}$$

where we define $\mathbb{A}^{|e}_{int} = d\boldsymbol{T}_{int}/d\boldsymbol{E}_e = d^2\Psi_{int}(\boldsymbol{E}_e)/(d\boldsymbol{E}_e d\boldsymbol{E}_e)$ as the hyperelastic logarithmic constitutive tensor in the intermediate configuration.

It is noted that the internal stress tensor $\boldsymbol{T}^{|e}_{int}$ depends on the same independent variables as $\boldsymbol{E}_e$, namely $\boldsymbol{E}$ and $\boldsymbol{F}_p$, and the internal flow stress $k = k(\gamma)$ is a function of the integral of

the plastic consistency parameter rate $\dot{\gamma}$—the equivalent plastic strain. The rate of the yield function may be formulated in two parts, using Eq. (4), as follows

$$\dot{f}_T = \dot{f}_T|_{\dot{\boldsymbol{F}}_p=\boldsymbol{0}} + \dot{f}_T|_{\dot{\boldsymbol{E}}=\boldsymbol{0}} \tag{21}$$

The first addend corresponds to the "trial elastic" contribution and may be obtained as

$$\tfrac{1}{2}\dot{f}_T|_{\dot{\boldsymbol{F}}_p=\boldsymbol{0}} = \nabla\phi_T : \dot{\boldsymbol{T}}^{|e}_{int}|_{\dot{\boldsymbol{F}}_p=\boldsymbol{0}} = \nabla\phi_T : \mathbb{A}^{|e}_{int} : {}^{tr}\dot{\boldsymbol{E}}_e \tag{22}$$

The second addend of Eq. (21) stands for a "corrector elastic" evolution and is obtained as:

$$\tfrac{1}{2}\dot{f}_T|_{\dot{\boldsymbol{E}}=\boldsymbol{0}} = -\dot{\gamma}\frac{1}{\frac{2}{3}k}(\nabla\phi_T : \mathbb{A}^{|e}_{int} : \nabla\phi_T + \tfrac{4}{9}k^2k') \tag{23}$$

Then, from the consistency condition $\dot{f}_T = 0$ when $\dot{\gamma} > 0$, we can have the following relation for the plastic consistency parameter

$$\dot{\Gamma} = \dot{\gamma}\frac{1}{\frac{2}{3}k} = \left(\frac{\mathbb{A}^{|e}_{int} : \nabla\phi_T}{\nabla\phi_T : \mathbb{A}^{|e}_{int} : \nabla\phi_T + \frac{4}{9}k^2k'}\right) : {}^{tr}\dot{\boldsymbol{E}}_e \quad \text{if} \quad \dot{\gamma} > 0 \tag{24}$$

And substituting Eq. (24) into Eq. (13), and defining

$$\hat{\boldsymbol{N}} = \frac{1}{\sqrt{\frac{2}{3}k}}\mathbb{N}_T : \boldsymbol{T}^{|e}_{int} \tag{25}$$

we have

$${}^{ct}\dot{\boldsymbol{E}}_e = -\left(\frac{\hat{\boldsymbol{N}} \otimes (\mathbb{A}^{|e}_{int} : \hat{\boldsymbol{N}})}{\hat{\boldsymbol{N}} : \mathbb{A}^{|e}_{int} : \hat{\boldsymbol{N}} + \frac{2}{3}k'}\right) : {}^{tr}\dot{\boldsymbol{E}}_e \quad \text{if} \quad \dot{\gamma} > 0 \tag{26}$$

Now, inserting Eq. (26) into Eq. (4), we obtain the relation between the elastic and its trial logarithmic strain rate tensor during plastic flow

$$\dot{\boldsymbol{E}}_e = \left(\mathbb{I}^S - \frac{\hat{\boldsymbol{N}} \otimes (\mathbb{A}^{|e}_{int} : \hat{\boldsymbol{N}})}{\hat{\boldsymbol{N}} : \mathbb{A}^{|e}_{int} : \hat{\boldsymbol{N}} + \frac{2}{3}k'}\right) : {}^{tr}\dot{\boldsymbol{E}}_e \quad \text{if} \quad \dot{\gamma} > 0 \tag{27}$$

Hence, the rate of internal stress can be rewritten as

$$\dot{\boldsymbol{T}}^{|e}_{int} = \mathbb{A}^{|e}_{ep} : {}^{tr}\dot{\boldsymbol{E}}_e \tag{28}$$

in which

$$\mathbb{A}^{|e}_{ep} = \mathbb{A}^{|e}_{int} - \frac{(\mathbb{A}^{|e}_{int} : \hat{\boldsymbol{N}}) \otimes (\mathbb{A}^{|e}_{int} : \hat{\boldsymbol{N}})}{\hat{\boldsymbol{N}} : \mathbb{A}^{|e}_{int} : \hat{\boldsymbol{N}} + \frac{2}{3}k'} \tag{29}$$

takes the widely-known standard form of infinitesimal elastoplasticity. Here, we interpret $\mathbb{A}^{|e}_{ep}$ as the internal continuum elastoplastic tangent tensor, lying in the actual intermediate

configuration. Using the relation between $\boldsymbol{T}_{int}$ and $\boldsymbol{T}^{|e}_{int}$, established in Eq. (11), the rate of the internal stresses tensor $\boldsymbol{T}_{int}$ in the reference configuration can be obtained by applying the chain rule of differentiation as

$$\dot{\boldsymbol{T}}_{int} = \dot{\boldsymbol{T}}^{|e}_{int} : \left.\frac{\partial \boldsymbol{E}_e}{\partial \boldsymbol{E}}\right|_{\dot{\boldsymbol{F}}_p=\boldsymbol{0}} + \boldsymbol{T}^{|e}_{int} : \frac{d}{dt}\left(\left.\frac{\partial \boldsymbol{E}_e}{\partial \boldsymbol{E}}\right|_{\dot{\boldsymbol{F}}_p=\boldsymbol{0}}\right) \tag{30}$$

The second term in Eq. (30) is the typical convective geometric term needed to obtain the relation of $\dot{\boldsymbol{T}}_{int}$ with $\dot{\boldsymbol{E}}$. However, for small steps, the convective term can be neglected, and for proportional loading, the term vanishes identically because it contains the derivative of the identity tensor. Then, by using Eqs. (3),(4) and (28) we can approximate

$$\begin{aligned}\dot{\boldsymbol{T}}_{int} &= \dot{\boldsymbol{T}}^{|e}_{int} : \left.\frac{\partial \boldsymbol{E}_e}{\partial \boldsymbol{E}}\right|_{\dot{\boldsymbol{F}}_p=\boldsymbol{0}} \\ &= \left.\frac{\partial \boldsymbol{E}_e}{\partial \boldsymbol{E}}\right|_{\dot{\boldsymbol{F}}_p=\boldsymbol{0}} : \mathbb{A}^{|e}_{ep} : \left.\frac{\partial \boldsymbol{E}_e}{\partial \boldsymbol{E}}\right|_{\dot{\boldsymbol{F}}_p=\boldsymbol{0}} : \dot{\boldsymbol{E}} = \mathbb{A}_{int} : \dot{\boldsymbol{E}}\end{aligned} \tag{31}$$

where we define $\mathbb{A}_{int}$ as the continuum elastoplastic moduli in the reference configuration by means of the pull-back operation over its internal counterpart $\mathbb{A}^{|e}_{int}$ in the intermediate configuration.

$$\mathbb{A}_{int} = \left.\frac{\partial \boldsymbol{E}_e}{\partial \boldsymbol{E}}\right|_{\dot{\boldsymbol{F}}_p=\boldsymbol{0}} : \mathbb{A}^{|e}_{ep} : \left.\frac{\partial \boldsymbol{E}_e}{\partial \boldsymbol{E}}\right|_{\dot{\boldsymbol{F}}_p=\boldsymbol{0}} \tag{32}$$

The complete set of equations of the anisotropic finite elastoplasticity model is summarized in Box 1.

2.2. Stress integration algorithm

The stress integration algorithm is simple. The purpose is to obtain the updated decomposition (see Fig. 2)

$${}^{t+\Delta t}_{0}\boldsymbol{F} = {}^{t+\Delta t}_{t}\boldsymbol{F}\,{}^{t}_{0}\boldsymbol{F} = {}^{tr}\boldsymbol{F}_e\,{}^{t}_{0}\boldsymbol{F}_p = {}^{t+\Delta t}_{0}\boldsymbol{F}_e\,{}^{t+\Delta t}_{t}\boldsymbol{F}_p^{-1}\,{}^{t+\Delta t}_{t}\boldsymbol{F}_p\,{}^{t}_{0}\boldsymbol{F}_p = {}^{t+\Delta t}_{0}\boldsymbol{F}_e\,{}^{t+\Delta t}_{0}\boldsymbol{F}_p \tag{33}$$

The integration of the *elastic* logarithmic strain rate tensor is immediately obtained using a *plain* backward-Euler algorithm

$$\begin{aligned}{}^{t+\Delta t}_{0}\boldsymbol{E}_e = {} & \underbrace{{}^{t}_{0}\boldsymbol{E}_e + \int_t^{t+\Delta t} {}^{tr}\dot{\boldsymbol{E}}_e d\tau}_{{}^{tr}\boldsymbol{E}_e := \frac{1}{2}\ln\left({}^{tr}\boldsymbol{F}_e^T\,{}^{tr}\boldsymbol{F}_e\right)} + \underbrace{\int_t^{t+\Delta t} {}^{ct}\dot{\boldsymbol{E}}_e d\tau}_{-\frac{3}{2}\left(\Delta\gamma/\,{}^{t+\Delta t}k\right)\mathbb{N}_T\,:\,{}^{t+\Delta t}\boldsymbol{T}^{|e}_{int}} \\ = {} & {}^{tr}\boldsymbol{E}_e - \frac{\Delta\gamma}{\frac{2}{3}\,{}^{t+\Delta t}k}\mathbb{N}_T : {}^{t+\Delta t}\boldsymbol{T}^{|e}_{int}\end{aligned} \tag{34}$$

Box 1: Anisotropic finite elastoplasticity model

1. Elastic logarithmic strain tensor obtained from the multiplicative decomposition

$$\boldsymbol{F}_e = \boldsymbol{F}_p^{-1}\boldsymbol{F}, \quad \boldsymbol{E}_e = \frac{1}{2}\ln(\boldsymbol{F}_e^T\boldsymbol{F}_e)$$

2. Elastic logarithmic strain rate tensor split

$$\dot{\boldsymbol{E}}_e = \dot{\boldsymbol{E}}_e|_{\dot{\boldsymbol{F}}_p=\boldsymbol{0}} + \dot{\boldsymbol{E}}_e|_{\dot{\boldsymbol{E}}=\boldsymbol{0}} = {}^{tr}\dot{\boldsymbol{E}}_e + {}^{ct}\dot{\boldsymbol{E}}_e$$

3. Generalized Kirchhoff stresses derived from the stored energy

$$\begin{aligned}\boldsymbol{T} &= \boldsymbol{T}_{kin} + \boldsymbol{T}_{int} \\ &= \frac{\Psi_{kin}(\boldsymbol{E})}{\boldsymbol{E}} + \underbrace{\frac{\Psi_{int}(\boldsymbol{E}_e)}{\boldsymbol{E}_e}}_{\boldsymbol{T}_{int}^{|e}} : \frac{\partial \boldsymbol{E}_e}{\partial \boldsymbol{E}}\end{aligned}$$

4. Evolution of the plastic flow

$${}^{ct}\dot{\boldsymbol{E}}_e = -\dot{\gamma}\frac{1}{\frac{2}{3}k}\nabla f_T = -\dot{\gamma}\frac{1}{\frac{2}{3}k}\mathbb{N}_T : \boldsymbol{T}_{int}^{|e} \neq -\dot{\boldsymbol{E}}_p$$

5. Yield function

$$f_T(\boldsymbol{T}_{int}^{|e}, k) = \boldsymbol{T}_{int}^{|e} : \mathbb{N}_T : \boldsymbol{T}_{int}^{|e} - \tfrac{2}{3}k^2 = 0$$

6. Loading/unloading condition

$$\dot{\gamma} \geq 0, \quad f_T(\boldsymbol{T}_{int}^{|e}, k) \leq 0, \quad \dot{\gamma} f_T(\boldsymbol{T}_{int}^{|e}, k) = 0$$

7. Relation between in-plane total and trial elastic logarithmic strains during plastic flow, with $\hat{\boldsymbol{N}} = \mathbb{N}_T : \boldsymbol{T}_{int}^{|e}/(\sqrt{\frac{2}{3}}k)$

$$\dot{\boldsymbol{E}}_e = \left(\mathbb{I}^S - \frac{\hat{\boldsymbol{N}} \otimes (\mathbb{A}_{int}^{|e} : \hat{\boldsymbol{N}})}{\hat{\boldsymbol{N}} : \mathbb{A}_{int}^{|e} : \hat{\boldsymbol{N}} + \frac{2}{3}k'}\right) : {}^{tr}\dot{\boldsymbol{E}}_e$$

8. Continuum elastoplastic tangent in the intermediate configuration

$$\mathbb{A}_{ep}^{|e} = \mathbb{A}_{int}^{|e} - \frac{(\mathbb{A}_{int}^{|e} : \hat{\boldsymbol{N}}) \otimes (\mathbb{A}_{int}^{|e} : \hat{\boldsymbol{N}})}{\hat{\boldsymbol{N}} : \mathbb{A}_{int}^{|e} : \hat{\boldsymbol{N}} + \frac{2}{3}k'}$$

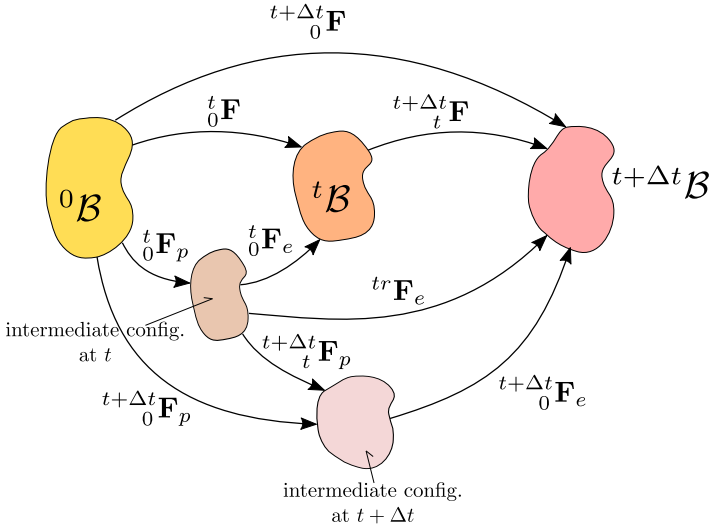

Figure 2: Multiplicative decomposition of the deformation gradient at $t+\Delta t$

where the algorithmic explicit definition of $^{tr}\boldsymbol{E}_e$ should be noted. Remarkably, the update formula is additive and identical to that of small strains. We do not explicitly employ the exponential mapping but, as it is obvious from the properties of the logarithmic strains, plastic flow is isochoric for pressure-insensitive yield criteria. Since stress and strains are not aligned in anisotropy, the previous equation must be solved iteratively using any algorithm typically employed in small strains [64]. For example, we establish the residuals

$$
\begin{aligned}
^{t+\Delta t}\mathsf{R} &= \begin{bmatrix} ^{t+\Delta t}\boldsymbol{\rho}_{int}\left(^{t+\Delta t}_{0}\boldsymbol{E}_e, \Delta\gamma\right) \\ ^{t+\Delta t}f_T\left(^{t+\Delta t}_{0}\boldsymbol{E}_e, \Delta\gamma\right) \end{bmatrix} \\
&= \begin{bmatrix} ^{t+\Delta t}_{0}\boldsymbol{E}_e - {}^{tr}\boldsymbol{E}_e + \dfrac{\Delta\gamma}{\frac{2}{3}\,^{t+\Delta t}k}\mathbb{N}_T : {}^{t+\Delta t}\boldsymbol{T}^{|e}_{int} \\ ^{t+\Delta t}\boldsymbol{T}^{|e}_{int} : \mathbb{N}_T : {}^{t+\Delta t}\boldsymbol{T}^{|e}_{int} - \frac{2}{3}\,^{t+\Delta t}k^2\left(^{t+\Delta t}\gamma\right) \end{bmatrix}
\end{aligned}
\tag{35}
$$

with $^{t+\Delta t}\boldsymbol{T}^{|e}_{int} = d\Psi_{int}/d\,^{t+\Delta t}_{0}\boldsymbol{E}_e = \mathbb{A}^{|e}_{int} : {}^{t+\Delta t}_{0}\boldsymbol{E}_e$. The equation $^{t+\Delta t}\mathsf{R} \longrightarrow \mathsf{O}$ is solved using a Newton-Raphson algorithm whose tangent is obtained as usual by straightforward algebra

$$
\begin{aligned}
\nabla^{t+\Delta t}\mathsf{R} &= \begin{bmatrix} \dfrac{d^{t+\Delta t}\boldsymbol{\rho}_{int}}{d\,^{t+\Delta t}_{0}\boldsymbol{E}_e} & \dfrac{d^{t+\Delta t}\boldsymbol{\rho}_{int}}{d\Delta\gamma} \\ \dfrac{d^{t+\Delta t}f_T}{d\,^{t+\Delta t}_{0}\boldsymbol{E}_e} & \dfrac{d^{t+\Delta t}f_T}{d\Delta\gamma} \end{bmatrix} \\
&= \begin{bmatrix} \mathbb{I}^S + \dfrac{\Delta\gamma}{\frac{2}{3}\,^{t+\Delta t}k}\mathbb{A}^{|e}_{int} & \dfrac{^{t+\Delta t}k - \Delta\gamma\,^{t+\Delta t}k'}{\frac{2}{3}\,^{t+\Delta t}k^2}\,^{t+\Delta t}\boldsymbol{T}^{|e}_{int} \\ 2\,^{t+\Delta t}\boldsymbol{T}^{|e}_{int} : \mathbb{N}_T : \mathbb{A}^{|e}_{int} & -\frac{4}{3}\,^{t+\Delta t}k\,^{t+\Delta t}k' \end{bmatrix}
\end{aligned}
\tag{36}
$$

with ${}^{t+\Delta t}k' = d\,{}^{t+\Delta t}k / d\,{}^{t+\Delta t}\gamma$ and $\mathbb{I}^S$ being the fourth order fully symmetric identity tensor.

As noted by Wali et al [65], an iterative procedure based on a single scalar parameter may be obtained immediately factoring-out the strain increment from the first equation and replacing the result in the second equation; i.e. after some algebra, for iteration (j)

$$ {}^{t+\Delta t}\gamma^{(j+1)} = {}^{t+\Delta t}\gamma^{(j)} - \frac{{}^{t+\Delta t}f^{(j)} - \dfrac{\partial\, {}^{t+\Delta t}f^{(j)}}{\partial\, {}^{t+\Delta t}_{0}\boldsymbol{E}_e} : \left(\dfrac{\partial\, {}^{t+\Delta t}\boldsymbol{\rho}^{(j)}_{int}}{\partial\, {}^{t+\Delta t}_{0}\boldsymbol{E}_e}\right)^{-1} : {}^{t+\Delta t}\boldsymbol{\rho}^{(j)}_{int}}{\dfrac{\partial\, {}^{t+\Delta t}f^{(j)}}{\partial\, {}^{t+\Delta t}_{0}\boldsymbol{E}_e} : \left(\dfrac{\partial\, {}^{t+\Delta t}\boldsymbol{\rho}^{(j)}_{int}}{\partial\, {}^{t+\Delta t}_{0}\boldsymbol{E}_e}\right)^{-1} : \dfrac{\partial\, \boldsymbol{\rho}^{(j)}_{int}}{\partial\Delta\gamma} + \dfrac{\partial\, {}^{t+\Delta t}f^{(j)}}{\partial\Delta\gamma}} \tag{37}$$

and using the known value of $\delta\gamma^{(j)} := {}^{t+\Delta t}\gamma^{(j+1)} - {}^{t+\Delta t}\gamma^{(j)}$ we can immediately update the elastic strains

$$ {}^{t+\Delta t}_{0}\boldsymbol{E}^{(j+1)}_e = {}^{t+\Delta t}_{0}\boldsymbol{E}^{(j)}_e - \left(\frac{\partial\, {}^{t+\Delta t}\boldsymbol{\rho}^{(j)}_{int}}{\partial\, {}^{t+\Delta t}_{0}\boldsymbol{E}_e}\right)^{-1} : \left[\, {}^{t+\Delta t}\boldsymbol{\rho}^{(j)}_{int} + \frac{\partial\, {}^{t+\Delta t}\boldsymbol{\rho}^{(j)}_{int}}{\partial\Delta\gamma}\delta\gamma^{(j)}\right] \tag{38}$$

This update is needed with hyperelastic relations and for actualization of the flow direction. Noteworthy, since in this case only $\partial^{t+\Delta t}\boldsymbol{\rho}^{(j)}_{int} / \partial^{t+\Delta t}_{0}\boldsymbol{E}_e = \left[\mathbb{I}^S + \frac{3}{2}(\Delta\gamma / {}^{t+\Delta t}k)\mathbb{A}^{|e}_{int}\right]$ must be inverted, and in metal plasticity $\mathbb{A}^{|e}_{int}$ may be considered constant (plastic strains are much larger than elastic ones), using Mandel notation [66], we can take advantage of the spectral decomposition of $\mathbb{A}^{|e}_{int}$ (performed only once during execution) to obtain a slightly faster algorithm. Indeed, in Mandel notation we have

$$\left[\left(\frac{\partial^{t+\Delta t}\boldsymbol{\rho}^{(j)}_{int}}{\partial\, {}^{t+\Delta t}_{0}\boldsymbol{E}_e}\right)^{-1}\right] = [\mathbf{Q}]\left(\left[\mathbf{I}^S\right] + \frac{\Delta\gamma}{\frac{2}{3}\, {}^{t+\Delta t}k}\left[\Lambda^{|e}_{int}\right]\right)^{-1}\left[\mathbf{Q}^T\right] \tag{39}$$

where $\left[\Lambda^{|e}_{int}\right]$ is the diagonal matrix of eigenvalues, $\left[\mathbf{I}^S\right]$ is the matrix representation of $\mathbb{I}^S$ (the identity matrix in Mandel notation) and $[\mathbf{Q}]$ is the matrix of eigenvectors of the matrix representation of $\mathbb{A}^{|e}_{int}$. Then, the inverse is obtained simply inverting a diagonal matrix and performing two matrix multiplications.

2.3. Consistent tangent

Once a solution has been obtained, following the standard steps of infinitesimal elastoplasticity, it is straightforward to obtain the elastoplastic *consistent* tangent of the Prandtl element, which takes exactly the same form as in the small strains case

$${}^{t+\Delta t}\mathbb{A}^{ep|tr}_{int} = \frac{d\, {}^{t+\Delta t}\boldsymbol{T}^{|e}_{int}}{d\, {}^{tr}\boldsymbol{E}_e} = {}^{t+\Delta t}\mathbb{D} - \frac{{}^{t+\Delta t}\mathbb{D} : {}^{t+\Delta t}\hat{\boldsymbol{N}} \otimes {}^{t+\Delta t}\mathbb{D} : {}^{t+\Delta t}\hat{\boldsymbol{N}}}{{}^{t+\Delta t}\hat{\boldsymbol{N}} : {}^{t+\Delta t}\mathbb{D} : {}^{t+\Delta t}\hat{\boldsymbol{N}} + \frac{2}{3}\, {}^{t+\Delta t}\varkappa'} \tag{40}$$

where ${}^{t+\Delta t}\mathbb{D}$ and ${}^{t+\Delta t}\varkappa$ are, respectively, the algorithmic elastic moduli and algorithmic uniaxial-like isotropic hardening defined also as in the infinitesimal framework

$$ {}^{t+\Delta t}\mathbb{D} = \mathbb{A}_{int}^{|e} : \left[\frac{d^{t+\Delta t}\boldsymbol{\rho}_{int}}{d\,{}^{t+\Delta t}_{0}\boldsymbol{E}_e} \right]^{-1} \quad \text{and} \quad {}^{t+\Delta t}\varkappa' = \frac{{}^{t+\Delta t}k\,{}^{t+\Delta t}k'}{{}^{t+\Delta t}k - \Delta\gamma\,{}^{t+\Delta t}k'} \tag{41} $$

As it can be checked immediately, if $\Delta\gamma \to 0$ then ${}^{t+\Delta t}\mathbb{D} \to \mathbb{A}_{int}^{|e}$ and ${}^{t+\Delta t}\varkappa' \to {}^{t+\Delta t}k'$.

The obtained solution for ${}^{t+\Delta t}_{0}\boldsymbol{E}_e$, ${}^{t+\Delta t}\boldsymbol{T}_{int}^{|e}$ and ${}^{t+\Delta t}\mathbb{D}$, must be transformed to the quantities usually handled by the finite element programs at the element level, for example ${}^{t+\Delta t}_{0}\boldsymbol{F}_p$, ${}^{t+\Delta t}\boldsymbol{S}$ and ${}^{t+\Delta t}\mathbb{C} := d\,{}^{t+\Delta t}\boldsymbol{S}/d\,{}^{t+\Delta t}_{0}\boldsymbol{A}$. To this end, considering small incremental steps, *for logarithmic strains*, we can make coincident the trial and final configurations just *for the task of performing mappings*. Note that this assumption holds exactly under proportional loads, so it is an approximation only for large steps and largely nonproportional loading. Then we can write ${}^{t+\Delta t}\boldsymbol{T}_{int}^{|e} \simeq {}^{t+\Delta t}\boldsymbol{T}_{int}^{|tr}$ (where $|e$ and $|tr$ implies the configuration where they live) and by systematic use of tensor mapping transformations [50]

$$ {}^{t+\Delta t}\boldsymbol{S}_{int} = {}^{t+\Delta t}\boldsymbol{S}_{int}^{|tr} : \frac{d^{tr}\boldsymbol{A}_e}{d\,{}^{t+\Delta t}_{0}\boldsymbol{A}} = {}^{t+\Delta t}\boldsymbol{T}_{int}^{|tr} : \frac{d^{tr}\boldsymbol{E}_e}{d\,{}^{t+\Delta t}_{0}\boldsymbol{A}} \tag{42} $$

where the mapping $d^{tr}\boldsymbol{E}_e/d\,{}^{t+\Delta t}_{0}\boldsymbol{A}$ is

$$ \frac{d^{tr}\boldsymbol{E}_e}{d\,{}^{t+\Delta t}_{0}\boldsymbol{A}} = \frac{d^{tr}\boldsymbol{E}_e}{d^{tr}\boldsymbol{A}_e} : {}^{t}_{0}\boldsymbol{F}_p^{-T} \odot {}^{t}_{0}\boldsymbol{F}_p^{-T} \tag{43} $$

Note that $d^{tr}\boldsymbol{E}_e/d^{tr}\boldsymbol{A}_e$ is known from the spectral decompositions of the involved strains [50]. Therefore

$$ {}^{t+\Delta t}\boldsymbol{S} = {}^{t+\Delta t}\boldsymbol{S}_{kin} + {}^{t+\Delta t}\boldsymbol{S}_{int} \tag{44} $$

and

$$ \begin{aligned} {}^{t+\Delta t}\mathbb{C} = & \left(\frac{d\,{}^{t+\Delta t}_{0}\boldsymbol{E}}{d\,{}^{t+\Delta t}_{0}\boldsymbol{A}} \right)^{T} : \mathbb{A}_{kin} : \frac{d\,{}^{t+\Delta t}_{0}\boldsymbol{E}}{d\,{}^{t+\Delta t}_{0}\boldsymbol{A}} + \boldsymbol{T}_{kin} : \frac{d^2\,{}^{t+\Delta t}_{0}\boldsymbol{E}}{d\,{}^{t+\Delta t}_{0}\boldsymbol{A} d\,{}^{t+\Delta t}_{0}\boldsymbol{A}} \\ & + \left(\frac{d^{tr}\boldsymbol{E}_e}{d\,{}^{t+\Delta t}_{0}\boldsymbol{A}} \right)^{T} : {}^{t+\Delta t}\mathbb{A}_{int}^{ep|tr} : \left(\frac{d^{tr}\boldsymbol{E}_e}{d\,{}^{t+\Delta t}_{0}\boldsymbol{A}} \right) + \boldsymbol{T}_{int}^{|e} : \frac{d^2\,{}^{tr}\boldsymbol{E}}{d\,{}^{t+\Delta t}_{0}\boldsymbol{A} d\,{}^{t+\Delta t}_{0}\boldsymbol{A}} \end{aligned} \tag{45} $$

where the third order tensors, containing the derivative of the mapping tensors, can be found, for example, in [50]. If we do not consider a constitutive equation for the uncoupled plastic spin, we can take ${}^{t+\Delta t}_{0}\boldsymbol{R}_e = {}^{tr}\boldsymbol{R}_e$ and the update of the plastic deformation gradient is

$$ {}^{t+\Delta t}_{0}\boldsymbol{F}_p = \exp\left(- {}^{t+\Delta t}_{0}\boldsymbol{E}_e \right) {}^{t+\Delta t}_{0}\boldsymbol{R}_e^{T}\, {}^{t+\Delta t}_{0}\boldsymbol{F} \tag{46} $$

The described implicit integration of this material model is summarized in Box 2 and has been implemented into a user material subroutine in ADINA program [67] via UCMAT3

user subroutine in dll format for the applications to sheet metal forming detailed below. We mention that ADINA provides an implicit integration scheme for global resolution (by defaut the Newton-Raphson method is used) with a Total Lagrangian formulation for large displacement/strain formulation. Therefore, in this case, we only need to return second Piola-Kirchhoff stress tensor $\boldsymbol{S}$ and its related consistent tangent modulus $\mathbb{C}$ to the main program.

3. Sheet metal forming applications

In this section, in order to use the u/p mixed formulation which is the default in ADINA to prevent locking in elastoplastic analyses, we propose that the total stored energy Ψ in Eq. (5) can be split into a volumetric hyperelastic part and a deviatoric elastoplastic part. Furthermore, the materials used in the sheet metal forming simulations below are considered elastically isotropic, so the stored energy contributions are quadratic in terms of the respective arguments, i.e.

$$\Psi(\boldsymbol{E},\boldsymbol{E}_e) = \underbrace{\frac{1}{2}\kappa(tr\boldsymbol{E}^v)^2 + \mu_{kin}\boldsymbol{E}^d:\boldsymbol{E}^d}_{\Psi_{kin}} + \underbrace{\mu_{int}\boldsymbol{E}_e^d:\boldsymbol{E}_e^d}_{\Psi_{int}} \tag{47}$$

where μ_{kin} and μ_{int} are the respective deviatoric, shear moduli (Lame's constant) of the external and internal part, respectively, and κ is the bulk modulus. $\boldsymbol{E}^v$ and $\boldsymbol{E}^d$ are the total volumetric and deviatoric logarithmic strain, respectively. $\boldsymbol{E}_e^d$ is internal deviatoric elastic logarithmic strain. Then, the elasticity nature are $\mathbb{A}_{kin} = \kappa\boldsymbol{I}\otimes\boldsymbol{I} + 2\mu_{kin}\mathbb{P}^S$ and $\mathbb{A}_{int} = 2\mu_{int}\mathbb{I}^S:\mathbb{P}^S$.

3.1. Drawing of a thin circular flange

The purpose of this example is to simulate the drawing process of a thin circular flange with a hole subjected to a prescribed radial displacement up to a total displacement of $u = 75$ mm at the inner rim as shown in Fig. 3a. The example is a simplified approach for the prediction of earing in cup drawing without using contact elements (which are usually the main source of convergence problems). This application is a benchmark for the response of anisotropic elastoplasticity based on the similar numerical problem considered in Refs. [68, 69, 29], among others. Our goal for this application is to compare the results obtained with our anisotropic elastoplasticity model based on the corrector elastic logarithmic strain rate with those obtained using an anisotropic additive elastoplasticity model in the logarithmic strain space based on Green plasticity [69], and also with those using the multiplicative decomposition with the flow rule in terms of the plastic strain rate, namely the Eterovic and Bathe algorithm [35] and the Caminero et al algorithm [29]. The whole circular flange is modelled in 3D using the 8-node bricks u/p mixed finite elements (in total 400 elements). Contact elements are not needed in this simulation because no out-of-plane drawing takes place. Only one layer of elements is considered through the thickness, while the in-plane discretization is shown in Fig. 3b.

The material is assumed to be isotropic in elastic response and orhotropic in its yield properties. The anisotropic plasticity is controlled by using Hill's yield criterion [70] through

Box 2: Implicit stress integration algorithm

1. Trial elastic predictor; geometric preprocessor: given ${}^{t+\Delta t}_{0}\boldsymbol{F}$, ${}^{t}_{0}\boldsymbol{F}_p$ and ${}^{t}_{0}\gamma$, compute the trial elastic predictor state

$$
\begin{aligned}
&{}^{tr}\boldsymbol{F}_p := {}^{t}_{0}\boldsymbol{F}_p; \quad {}^{tr}\boldsymbol{F}_e := {}^{t+\Delta t}_{0}\boldsymbol{F}\,{}^{t}_{0}\boldsymbol{F}_p^{-1}\\
&{}^{tr}\boldsymbol{E}_e := \frac{1}{2}\ln({}^{tr}\boldsymbol{F}_e^{T\,tr}\boldsymbol{F}_e); \quad {}^{tr}\boldsymbol{T}^{|e}_{int} := \frac{d\Psi_{int}({}^{tr}\boldsymbol{E}_e)}{d\,{}^{tr}\boldsymbol{E}_e}
\end{aligned}
$$

2. Check yield condition and test for plastic loading

$$
\begin{aligned}
&{}^{tr}k := {}^{t}k\\
&{}^{tr}f_T := f_T({}^{tr}\boldsymbol{T}^{|e}_{int}, {}^{tr}k) = {}^{tr}\boldsymbol{T}^{|e}_{int} : \mathbb{N}_T : {}^{tr}\boldsymbol{T}^{|e}_{int} - \tfrac{2}{3}{}^{tr}k^2
\end{aligned}
$$

IF ${}^{tr}f_T \leq 0$ THEN

Elastic step: set ${}^{t+\Delta t}(\bullet) = {}^{tr}(\bullet)$

ELSE

Plastic step: Proceed to step 3

ENDIF

3. Return mapping
   (a) Local Newton iterations: plastic corrector

   Solve iteratively $\mathsf{R}({}^{t+\Delta t}\boldsymbol{E}_e, \Delta\gamma) = \begin{Bmatrix} {}^{t+\Delta t}\boldsymbol{\rho} \\ {}^{t+\Delta t}f_T \end{Bmatrix} = \boldsymbol{0}$ using the Newton-Raphson method with initial values for first iteration ${}^{t+\Delta t}\boldsymbol{E}_e^{(0)} = {}^{tr}\boldsymbol{E}_e$, $\Delta\gamma^{(0)} = 0$ and ${}^{t+\Delta t}k^{(0)} = k({}^{t}\gamma)$

   (b) Update the state variables

$$
{}^{t+\Delta t}\boldsymbol{T}^{|tr}_{int} \simeq {}^{t+\Delta t}\boldsymbol{T}^{|e}_{int} = \left.\frac{d\Psi_{int}(\boldsymbol{E}_e)}{d\boldsymbol{E}_e}\right|_{t+\Delta t}
$$

   Perform mappings to desired stress/strain quantities, e.f compute the consistent elastoplastic tangent matrix during this phase (see Box 3)

   (c) Compute consistent tangent and update plastic deformation gradient ${}^{t+\Delta t}_{0}\boldsymbol{F}_p$ as explained in Sec. 2.3
4. Perform mappings to the desired stress and strain quantities, e.g. ${}^{t+\Delta t}\boldsymbol{S}$ and ${}^{t+\Delta t}_{0}\boldsymbol{A}$ in the case of Total Lagrangian formulations.
5. EXIT

the deviatoric tensor $\mathbb{N}_T$ in Eq. (17) according to Ref. [8]. Two cases are considered for anisotropic plasticity. In case I, it is expected that the plastic strain is concentrated at 45^o

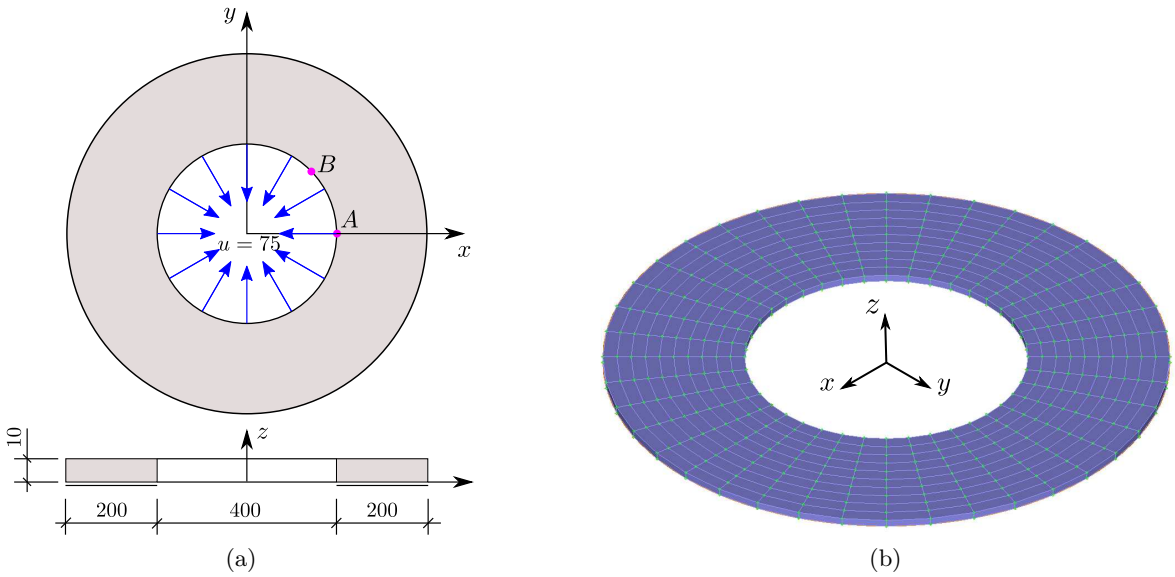

Figure 3: Drawing of a thin circular flange: a) geometry and boundary conditions b) FE discretization. All dimensions are in mm.

and 135^o from the x-axis along the direction of the maximum shear stress; while in case II the plastic strain is expected to concentrate along the x and y axes. In both cases, linear isotropic hardening is assumed. In examples below it is combined with the Voce-type non-linear isotropic hardening function [71] in the form:

$$k = k_0 + \bar{H}\gamma + (k_\infty - k_0)(1 - e^{-\delta\gamma}) \tag{48}$$

where γ is the equivalent accumulated plastic logarithmic strain, see Eq. (15). The material parameters of the metal-sheet are identical to those used in Refs. [68, 69] and are given in Table 1. Thus, only the flow kinematics and the type of finite element used are different between the approaches, which makes this comparison especially interesting.

Fig. 4 shows the deformed flanges with the distribution of the accumulated plastic strains for different cases and compared with those obtained in Ref. [69] and also with simulations performed using either the model of Caminero et al [29] or the Eterovic and Bathe model [35] (for the case of *elastic* isotropy both models give the same results as shown in Ref. [29]). It is noted that the results obtained in both references [69, 29] are also without contact/friction. It can be observed that the deformations and distributions of accumulated plastic strains obtained in this work are very similar to those obtained in the other references, so the small differences may not be necessarily attributed to the plasticity formulation because in Ref. [69] the authors used a mixed shell element with incompatible modes. In case I the plastic strains are produced and concentrated in the directions of maximum shear stresses at 45^o and 135^o from x-axis and in case II the maximum plastic strains occur in directions of maximum normal stresses at x and y axes as expected. For both cases, the outer rim is deformed in the a well-known *earing* shape of anisotropic sheet metal forming.

The nodal forces acting at the two nodes A and B depicted in Fig. 3a are also extracted

Table 1: Material parameters for drawing of a thin circular flange

Bulk modulus	$\kappa = 164.20$ GPa
Internal shear moduli	$\mu_{int} = 80.19$ GPa
Reference yield stress	$k_0 = 0.45$ GPa
Limit stress parameter	$k_\infty = 0.45$ GPa
Voce's linear hardening modulus	$\bar{H} = 0.1$ GPa
Voce hardening parameter	$\delta = 1$
Hill's anisotropy parameters - Case I	
$f = g = h$	$1/3$
$l = m = n$	4
Hill's anisotropy parameters - Case II	
$f = g = h$	$1/3$
$l = m = n$	$1/4$

in order to compare with those obtained in Ref. [69] (note that we used an equivalent mesh to perform this comparison). Fig. 5 depicts this comparison of the nodal forces for both cases. It can be observed that the nodal forces obtained in this work are close to those obtained in Ref. [69], specially for case I. A difference can be observed for case II (see Fig. 5b) at the maximum value of the nodal force at the point B. As already mentioned in [69], the classical multiplicative decomposition gives a similar peak as the Green-additive plasticity of Reference [69]. It is not clear the source of this difference, but one of the possible causes may be the different flow rule employed. Note that our flow rule is written in terms of corrector elastic strains derived from the chain rule, in a similar approach as isotropic plasticity based on the Lie derivative (e.g. [31, 11]) but employing logarithmic strains, whereas classical flow rules in anisotropy are based on the evolution of plastic quantities (e.g. [69, 72, 43, 36, 9, 29, 35], among many others). The type of element may also have some impact since incompatible elements as the ones used in Ref. [69] may give softer responses. Finally, typical convergence rates of the algorithm for this example are shown in Table 2 (local algorithm) and in Figure 6 (global iterations from ADINA).

Table 2: Thin circular flange. Typical local convergence rates for the plasticity model presented in this work

Local iterative algorithm		
Step/Iteration	$\boldsymbol{\rho}_{int}$ residuals	f_T residual
$2/0$	$1.000E+00$	$1.000E+00$
$2/1$	$5.968E-03$	$1.218E-02$
$2/2$	$5.492E-07$	$5.562E-07$
$2/3$	$2.789E-15$	$1.264E-16$
$90/0$	$1.000E+00$	$1.000E+00$
$90/1$	$4.496E-03$	$1.118E-02$
$90/2$	$5.126E-07$	$5.325E-07$
$90/3$	$1.896E-15$	$1.059E-16$

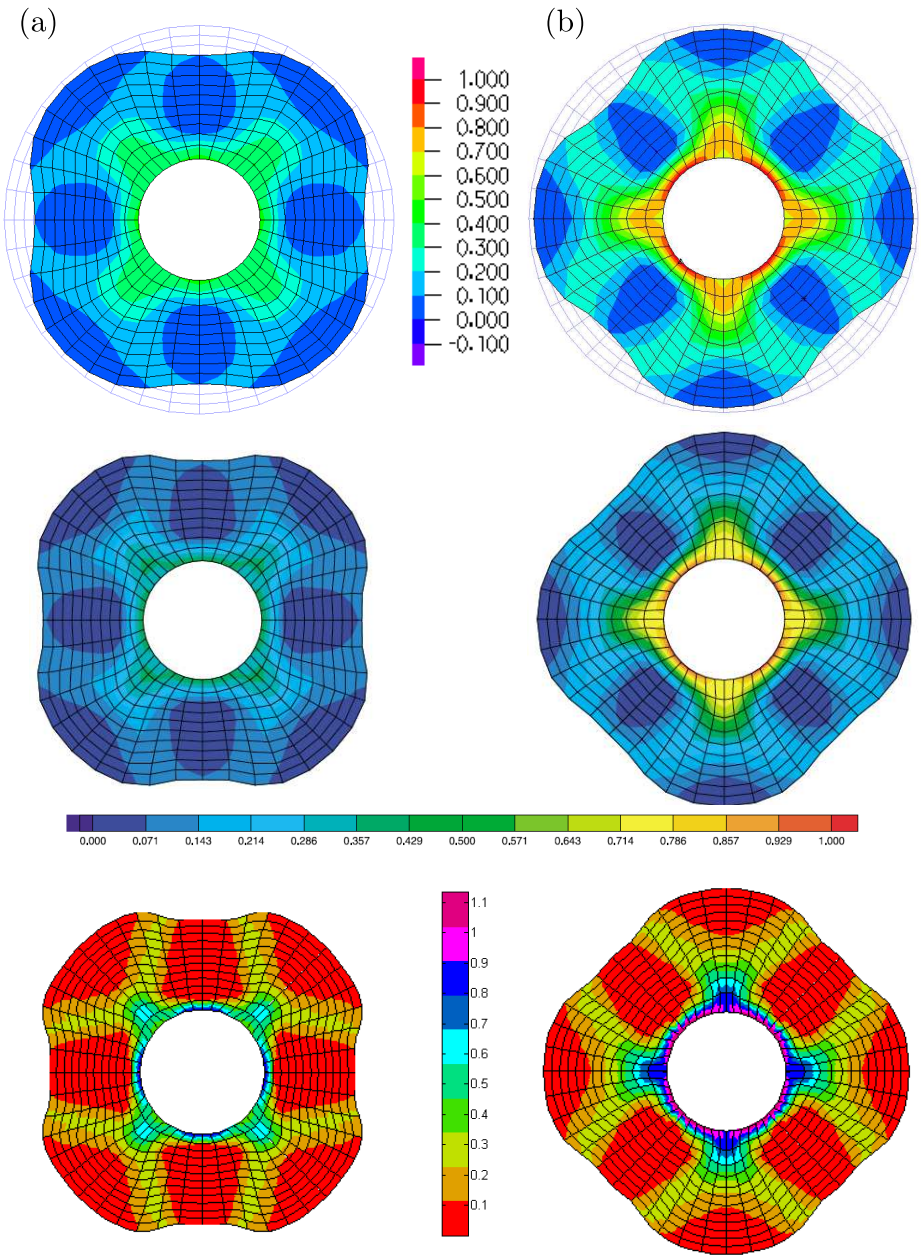

Figure 4: Comparison of the accumulated plastic strain for two cases in the final deformed configuration: a) case I; b) case II. Top row figures show the results of the present model, second row figures show the results obtained in Ref. [69] (with permission from Elsevier), whereas bottom row figures are the results obtained in Ref. [29] (with permission from Elsevier) using additive Green plasticity for either the Eterovic-Bathe algorithm or Caminero et al. 2011 [29] algorithm.

3.2. Cylindrical cup drawing

The second benchmark test is the simulation of a 3D cylindrical cup drawing process, which is an important process in the field of the sheet metal forming and has been usually

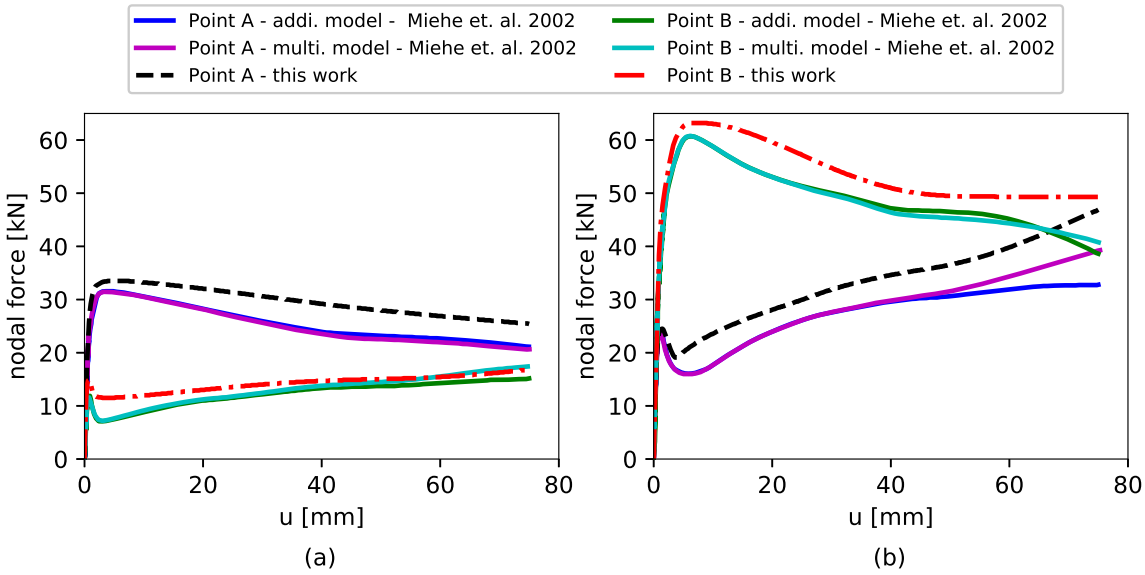

Figure 5: Comparison of the nodal forces at two points A and B obtained in this work with those obtained by [69]: a) case I and b) case II

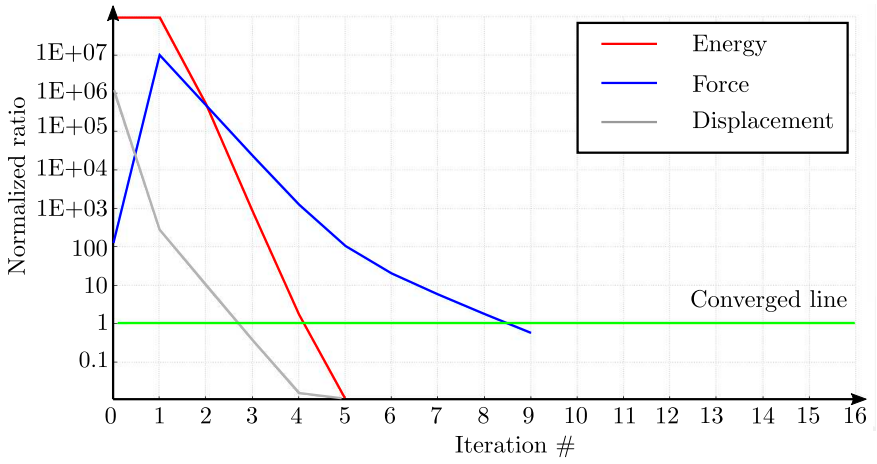

Figure 6: Typical global convergence rates obtained from ADINA

used to demonstrate the capabilities of the material models [73, 74, 69, 75, 28, 49]. A sketch of the specimen with its geometric dimensions is shown in Fig. 7a. The material for this case is an Al-Mg aluminum alloy (Al-5 wt% Mg), which is the same material used in the experimental analysis in Ref. [75] and in the subsequently in numerical simulation in Ref. [28]. Orthotropic plasticity is introduced using the Hill yield criterion through the proper tensor $\mathbb{N}_T$, and the Voce-type nonlinear isotropic hardening is only considered. For comparison purposes, we

have employed the same (i.e. equivalent) material parameters as in Refs. [75, 28]. These material parameters are summarized in Table 3.

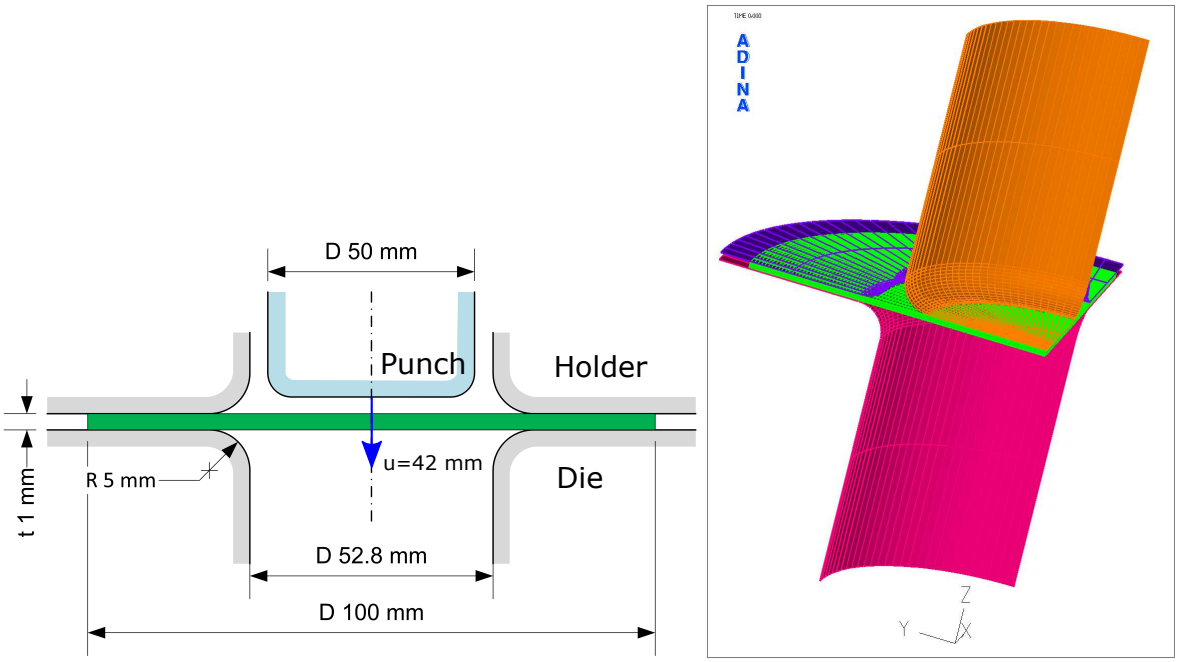

(a) (b)

Figure 7: Sketch of the cylindrical cup drawing and its FE model

Table 3: Material parameters of Al-5 wt% Mg

Bulk modulus	$\kappa = 68,627.47$ MPa
Internal shear moduli	$2\mu_{int} = 26,315.8$ MPa
External shear moduli	$2\mu_{kin} = 0$ MPa
Isotropic hardening Voce's parameters	
Reference yield stress	$k_0 = 85.4$ MPa
Limit stress parameter	$k_\infty = 336.2$ MPa
Voce's linear hardening modulus	$\bar{H} = 0$ MPa
Voce hardening parameter	$\delta = 6.242$
Hill's anisotropy parameters	
f	0.534
g	0.634
h	0.418
$l = m$	1.50
n	1.97

Only a quarter part of the cup is modelled due to both geometric and material symmetry

conditions (see Fig. 7b). The blank is discretized in 8-node bricks Q1/P0 u/p mixed finite elements (in total 4312 elements), while the punch, the holder and the die are modelled as rigid bodies. Different contact pairs are established between the blank and the rigid tool elements. A coefficient of 0.1 is assumed for the friction between these contact pairs. The numerical simulation is performed in ADINA [67] (using the material user subroutine) with a prescribed displacement of the punch to 42 mm.

Fig. 8 shows the accumulated plastic strains of the deformed cup at different states of the drawing process, together with the appearance of the typical ears. At the final deformed configuration, the earing profile is obtained and compared with the experimental earing profile given in Ref. [75] and the simulated earing profile given in Refs. [75, 28]. Fig. 9a depicts this comparison. It can be seen that the earing profile obtained in this work fits better the measured earing in the experiments, in particular, the height of the earing at the angles (0°, 45°, 75° and 90°) are very close to the experimental points. The model used in Ref. [75] only fits well the experiments at the peak (90°), while the proposed model of Ref. [28] only predicts well the height at angle 45°. For other angles, the models of Refs. [75] and [28] present less accurate results than the present formulation. A remarkable observation from Fig. 9a is that the predictions in Refs. [75] and [28] where not able to capture well the experimental earing, neither with a Hill criterion nor with a Barlat Yld2000-2D criterion. However, our simulation, using the Hill criterion with the same parameters was able to capture fairly well the experimentally observed earing.

The equivalent punch force applied during the drawing process is also obtained and compared with those obtained in Ref. [28] as shown in Fig. 9b. A similar punch force is predicted in both works.

Fig. 10a shows the yield stress and the r-value of anisotropy predicted by our model and compared with those obtained from the experimental [75] and by the numerical simulation in Ref. [28]. It is observed that the prediction of the yield stress with respect to the angle from the rolling direction is similar to that obtained in Ref. [28] (where equivalent parameters were used), while the r-values of anisotropy predicted by our model also differ from the experimental data, but are similar to those obtained in Ref. [28]. Since both models use the same constants and no rotations are involved, similar values are obtained with both formulations as expected, and the discrepancy seems to be due to the actual material parameters or possibly due to the yield function, not to the specific formulation employed.

3.3. Square cup drawing

In this example, we show simulations of the square cup drawing process. The specimen for the numerical simulation is similar to the NUMISHEET93 benchmark example for aluminum alloy [76]. The initial flat aluminum sheet of $150 \times 150 \times 0.81$ mm is placed between the blank-holder and the die as shown in Fig. 11. In order to perform comparisons, the material parameters are also obtained from Ref. [28] and are summarized in Table 4.

Due to the symmetry of the geometry and to the orthotropy of the material, a quarter of the blank is modelled again using 8-node bricks Q1/P0 u/p mixed finite elements (see Fig. 11). In this example, we also want to analyse the relevance of the bending effect on the accumulated plastic strain during the drawing process. Therefore, two simulations have been performed: one simulation with one element in the thickness of the blank (NS1) and other

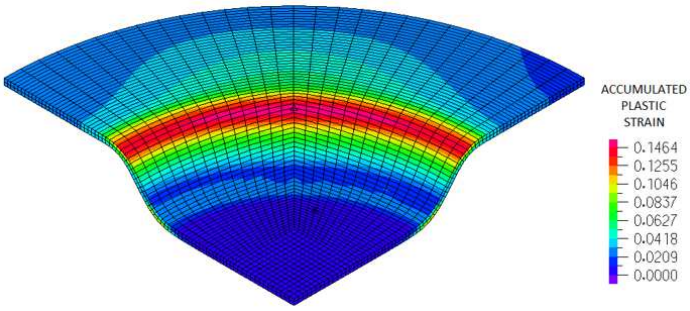

(a) u=7.5 mm

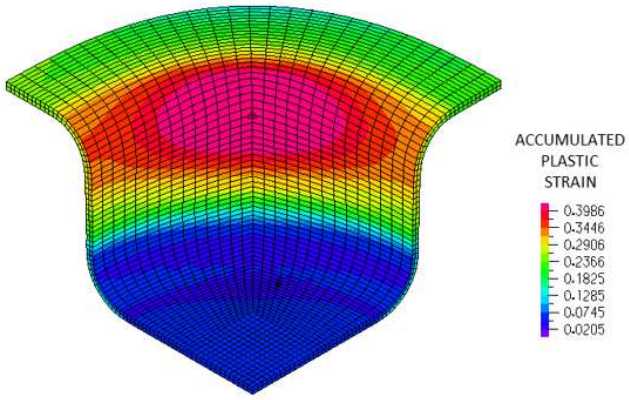

(b) u=22 mm

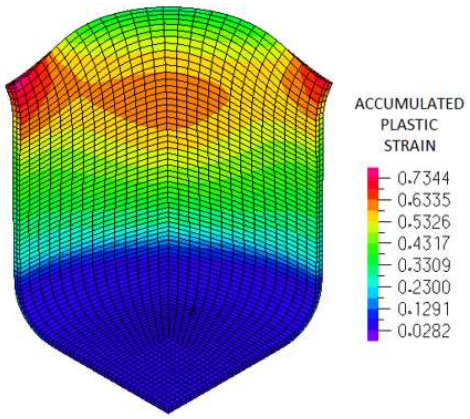

(c) u=32 mm

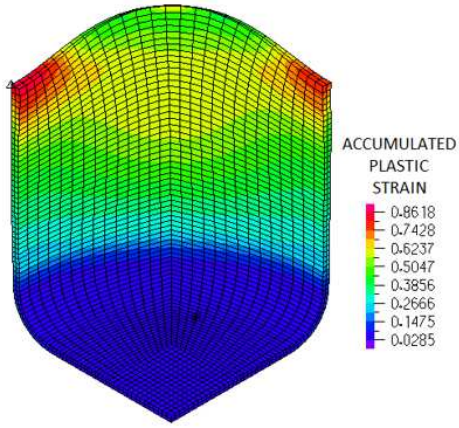

(d) u=42 mm

Figure 8: Accumulated plastic strain at different punch displacements of cylindrical drawing

with two elements in the thickness (NS2). A prescribed displacement of 15 mm is applied for the punch, while a constant force of 4.9 kN is applied for the blank-holder.

Figs. 12 and 13 show the contour plots of the von Mises stress and the accumulated plastic strain at the final deformed configuration of the blank, respectively, and compared with the

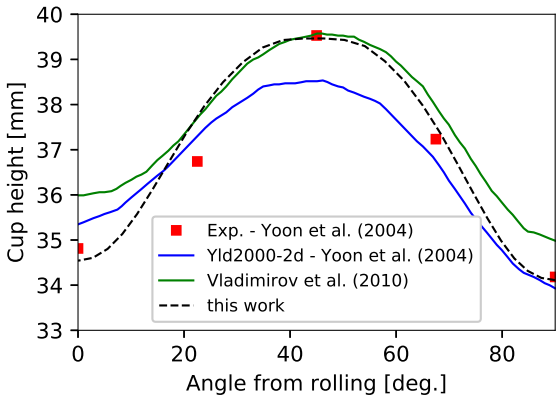

(a) Comparison of earing profiles

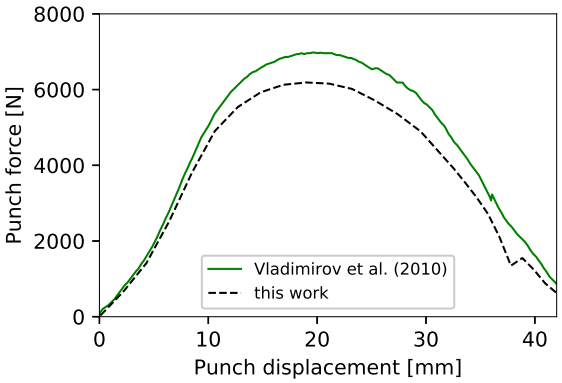

(b) Comparison of punch force

Figure 9: Comparison of results

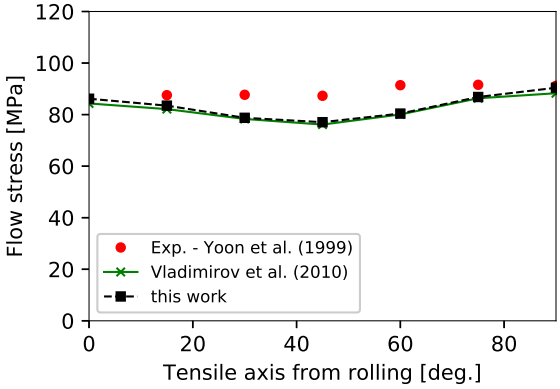

(a) Yield stress

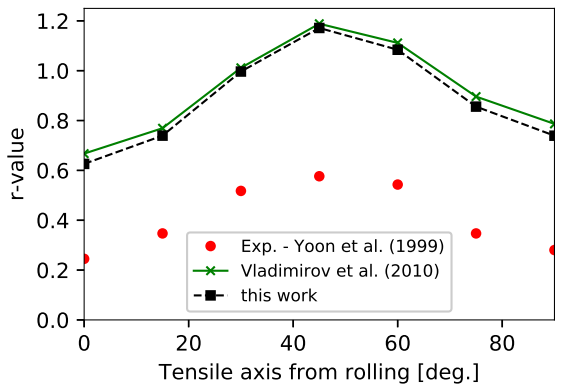

(b) r-value anisotropy

Figure 10: Comparison of the yield stress and r-value

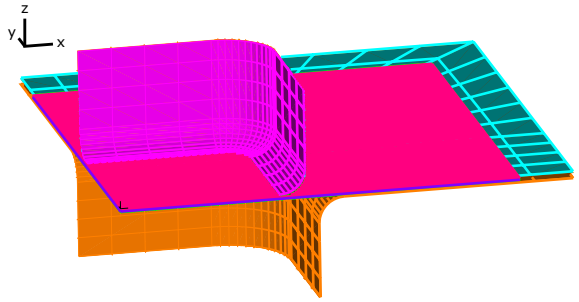

Figure 11: FE model for square cup drawing

Table 4: Material parameters for Numisheet93 aluminum alloy

Bulk modulus	$\kappa = 68,627.47$ MPa
Internal shear moduli	$2\mu_{int} = 26,315.8$ MPa
External shear moduli	$2\mu_{kin} = 0$ MPa
Isotropic hardening Voce's parameters	
Reference yield stress	$k_0 = 137.5$ MPa
Limit stress parameter	$k_\infty = 351.5$ MPa
Voce's linear hardening modulus	$\overline{H} = 0$ MPa
Voce hardening parameter	$\delta = 9.75$
Hill's anisotropy parameters	
f	0.52
g	0.51
h	0.508
$l = m$	1.50
n	1.64

results obtained by Ref. [28]. Note that there is a visual effect because the view of our plots is an axonometric view (parallel lines remain parallel in the view), whereas the view of Ref. [28] is in conic perspective (with a vanishing point) with a different inclination. However, the specimens of both works have the same dimensions, taken from Ref. [74]. It can be observed that the maximum von Mises stress and the accumulated plastic strains are at the punch shoulder similar to the result of Ref. [28]. The values of von Mises stresses obtained with our models are similar to those of Ref. [28]. However, the accumulated plastic strain takes different values in our simulation respect to those of Ref. [28]. This difference is due to the fact that both formulations are different, and also possibly because the type of elements that is used in our model is different. In particular, in our models 8-node Q1/P0 brick mixed u/p finite elements (ADINA standard) have been used for the blank, while the C3D8R element with reduced integration (ABAQUS element) has been used in Ref. [28]. Our results are larger probably because of bending effects. Furthermore, the result from the model using one element through the thickness is very similar to the result using two elements in thickness, so using Q1/P0 elements, one element through the thickness may be sufficient to capture the behavior because the problem is dominated by the membrane effects.

The amounts of draw-in in three directions, DX (rolling direction), DY (transverse direction) and DD (diagonal direction), are obtained and compared with those obtained from the experiment [74] and those obtained in Ref. [28], and are listed in Table 6. Our results for DX and DY are slightly higher than the observed experimental values, while slightly lower for DD. However, errors are in all cases below 10%. In this case, contact formulations may also be the source of some discrepancies.

3.4. S-rail forming

The present benchmark, so-called S-rail forming, was proposed in the NUMISHEET 1996 International Conference [77]. It consists in the forming of a plane metal blank into a final

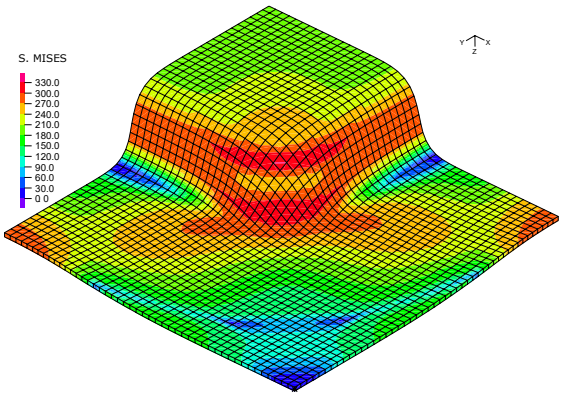

(a) 1 element in blank thickness

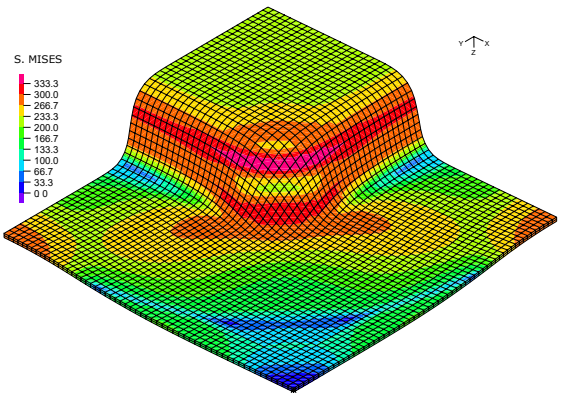

(b) 2 elements in blank thickness

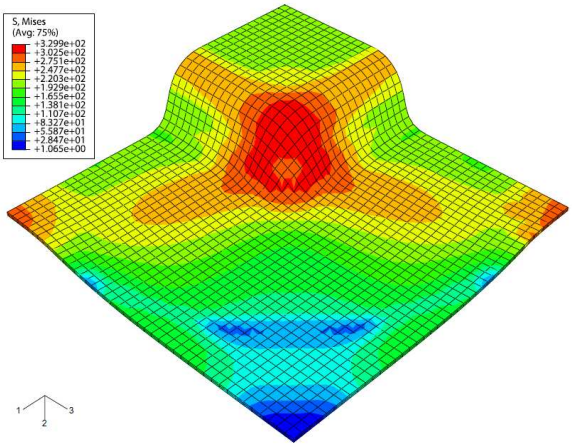

(c) Vladimirov et al. (2010) (with permission from Elsevier)

Figure 12: Square cup drawing: comparison of von Mises stress between the present model and that of Ref. [28]

Table 5: Amount of draw-in

Description	Experiment in [74]	FE results from [28]	Model NS1	Model NS2
DX (X-direction)	5.3	5.01	5.63	5.66
DY (Y-direction)	5.4	5.05	5.67	5.69
DD (Diagonal dir.)	3.0	2.59	2.76	2.78

component with a S-shaped 3D geometry by deep drawing. Due to the complex geometry of this problem, this simulation is an interesting validation, specially about the possible presence of wrinkles. The geometry of the blank, die, punch and blank-holder are extracted from the conference proceedings, Ref. [77]. Initially, the blank has a thickness of 0.92 mm and is

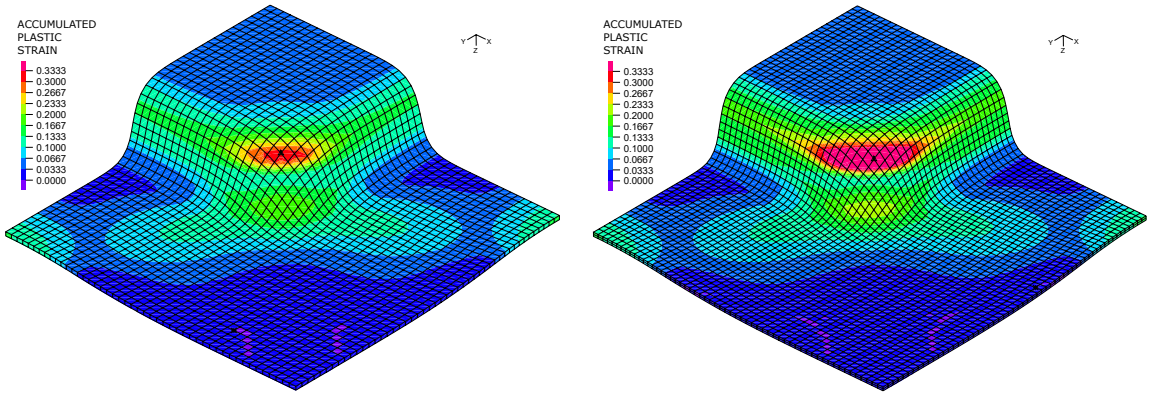

(a) 1 element in blank thickness

(b) 2 elements in blank thickness

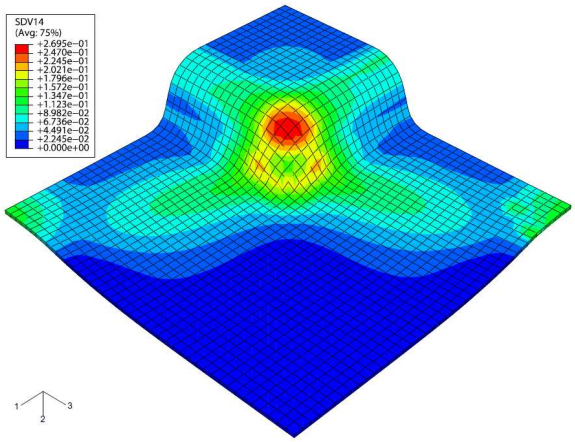

(c) Vladimirov et al. (2010) (with permission from Elsevier)

Figure 13: Square cup drawing: comparison of accumulated plastic strain between our results and result of [28]

mounted between the die and the blank-holder. The punch is moved upward until a total displacement of 37 mm, while a constant force of 10 kN is applied on the blank-holder. In this application we focus on the springback wrinkling prediction, since this effect is not normally mentioned in other works [78, 27, 28, 79], but is present in experimental tests [80, 81, 82].

The numerical simulation is performed again in ADINA using our material subroutine [67]. The punch, die and blank-holder are rigid bodies, while the blank is discretized by 8-node Q1/P0 mixed u/p finite elements (in total 6000 elements). The contacts are established between the tools and the blank until the punch displacement reaches 37 mm. Thereafter, the contacts between the blank and the die, between the blank and the punch, are removed. The contact between the blank and the blank-holder is maintained for spring-back of the blank. The material used for the blank is a draw quality mild interstitial free (IF) steel with its identified parameters listed in Table 6, taken from Ref. [77]. Coulomb's coefficient of

friction of 0.11 is considered for all surfaces in contact. Figs. 14a and 14b show the schematic view of the tools and the adopted mesh, respectively.

Table 6: Material parameters for IF steel

Bulk modulus	$\kappa = 171,666.67$ MPa
Internal shear moduli	$2\mu_{int} = 157,142$ MPa
External shear moduli	$2\mu_{kin} = 1,320$ MPa
Isotropic hardening Voce's parameters	
Reference yield stress	$k_0 = 152$ MPa
Limit stress parameter	$k_\infty = 297$ MPa
Voce's linear hardening modulus	$\bar{H} = 0$ MPa
Voce hardening parameter	$\delta = 4.5$

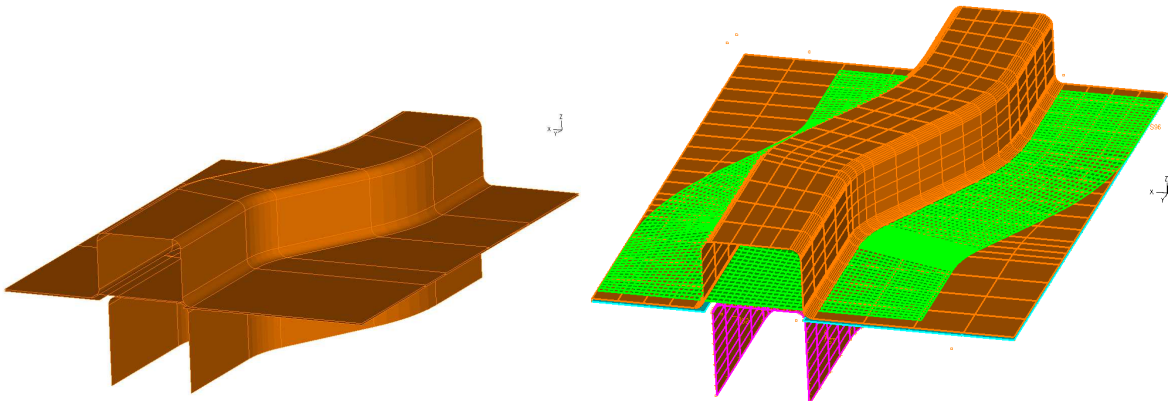

(a) Tools (b) FE model

Figure 14: S-Rail drawing process

Fig. 15a shows the deformed configuration of the blank for the maximum punch displacement. It can be seen that the wrinkle appearance is visible at the curved parts as expected [80, 81, 82]. The contour of von Mises stress is also depicted in Fig. 15b.

The equivalent force applied on the punch during the forming process is also obtained and compared with those measured in the experiment and by the numerical simulation given in Ref. [27] as shown in Fig. 16. It is noted that our result over-predicts the experimental data, specially in a range from 5 to 20 mm of punch displacement, but the final force is very close to the one measured in the experiment. The source of the discrepance is unknown, but is not necessarily attributable to the material model, since the type of elements for the blank, and contact element formulations, may affect significatively the results, specially during the initial stages where contact conditions have the most influences, since the interaction surface blank-holder is larger.

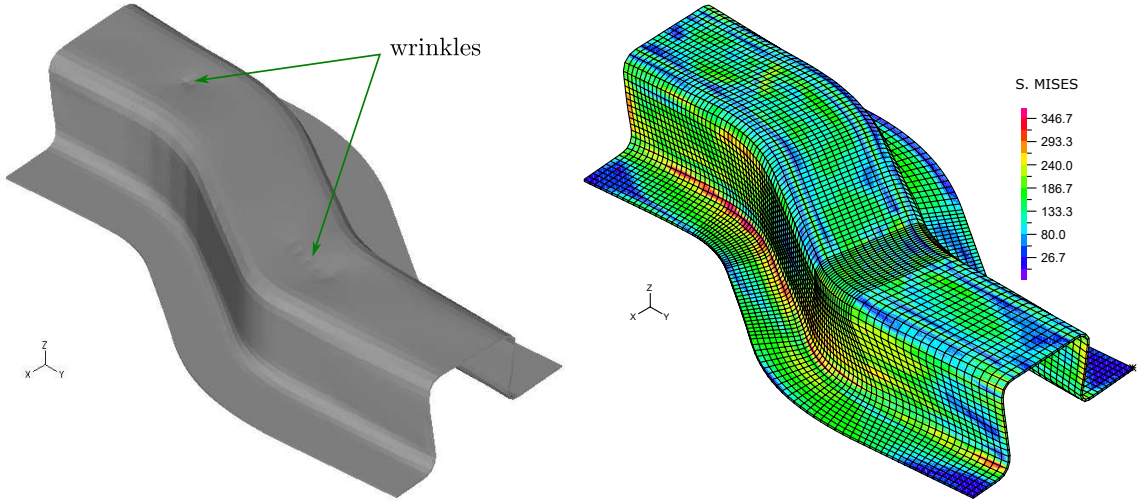

(a) Deformed blank after springback (b) Residual von Mises stress after springback

Figure 15: S-rail simulation at the end of forming

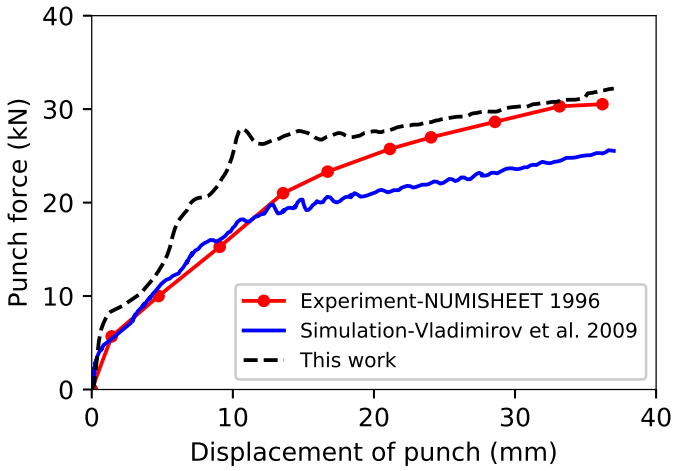

Figure 16: S-rail simulation: comparison of the punch force during S-rail forming

4. Conclusions

To avoid spurious dissipation, large strain formulations for elastoplasticity should be based on exactly-integrable elastic and kinematic hardening behaviors. Hyperelasticity is the simplest way to achieve this. The state variables entering the stored energy may be obtained either from additive Green-plasticity ansatzes or from multiplicative plasticity, the latter being the usually preferred approach, as explained in the Introduction Section. Unfortunately, in the case of anisotropy, the use of the multiplicative decomposition has resulted in complex formulations which depart from the infinitesimal theory.

However, the use of the chain rule brings naturally elastic corrector rates into the dissipation equation, which in turn motivates flow rules in terms of these rates instead of in terms of rates of plastic quantities. Remarkably, this novel formulation results in an additive framework identical to that of the small strains theory abiding by the accepted multiplicative decomposition. In this formulation, the treatment of anisotropic elasto-plasticity presents no difficulty, the Mandel stress tensor is not present, and plastic spin is uncoupled.

An important issue which we have herein addressed is the performance of the formulation in metal forming simulations, and how the results using the novel flow rule compare with established theories. From the simulations performed, we can conclude that the algorithmic formulation is robust for performing complex simulations in industry, and that the theory gives overall comparable results to those obtained using other approaches. Then, the simplicity and generality of the proposed multiplicative large strain formulation is promising for the incorporation of further features in a setting which is simple and remarkably similar to the infinitesimal theory.

Acknowledgments

Partial financial support for this work has been given by grant PGC 2018-097257-B-C32 from the Dirección General de proyectos de Investigación of the Ministerio de Economía y Competividad of Spain. The ADINA program license used in this work has been a courtesy of ADINA R&D to the UPM.

References

[1] R. Wagoner, J.-L. Chenot, Metal forming analysis, Cambridge University Press, Cambridge, 2001.

[2] J. Hu, Z. Marciniak, J. Duncan, Mechanics of sheet metal forming, Elsevier, 2002.

[3] M. James, Residual stress influences on structural reliability, Engineering Failure Analysis 18 (8) (2011) 1909–1920.

[4] F. Neukamm, M. Feucht, A. Haufe, Considering damage history in crashworthiness simulations, Ls-Dyna Anwenderforum.

[5] G. D'Amours, A. Rahem, B. Williams, M. Worswick, R. Mayer, Crashworthiness of aluminium tubes; part 1: Hydroforming at different corner-fill radii and end feeding levels, in: AIP Conference Proceedings, Vol. 908, AIP, 2007, pp. 787–792.

[6] P. Hosseini-Tehrani, E. Asadi, Effects of new materials on the crashworthiness of s-rails, Proceedings of the Institution of Mechanical Engineers, Part L: Journal of Materials: Design and Applications 222 (1) (2008) 37–44.

[7] G. Miscia, V. Rotondella, A. Baldini, E. Bertocchi, L. DAgostino, Aluminum structures in automotive: Experimental and numerical investigation for advanced crashworthiness, in: ASME 2015 International Mechanical Engineering Congress and Exposition, American Society of Mechanical Engineers, 2015, pp. V012T15A013–V012T15A013.

[8] M. Kojic, K.-J. Bathe, Inelastic Analysis of Solids and Structures, Springer-Verlag Berlin Heidelberg, 2005.

[9] A. Shutov, J. Ihlemann, Analysis of some basic approaches to finite strain elasto-plasticity in view of reference change, International Journal of Plasticity 63 (2014) 183–197.

[10] K.-J. Bathe, Finite Element Procedures, 2nd Ed, Klaus-Jürgen Bathe, 2014.

[11] J. C. Simo, T. J. Hughes, Computational inelasticity, Vol. 7, Springer Science & Business Media, 2006.

[12] T. J. Hughes, J. Winget, Finite rotation effects in numerical integration of rate constitutive equations arising in large-deformation analysis, International journal for numerical methods in engineering 15 (12) (1980) 1862–1867.

[13] W. Rolph III, K.-J. Bathe, On a large strain finite element formulation for elasto-plastic analysis, Constitutive Equations: Macro and Computational Aspects.

[14] G. C. Johnson, D. J. Bammann, A discussion of stress rates in finite deformation problems, International Journal of Solids and Structures 20 (8) (1984) 725–737.

[15] A. Meyers, H. Xiao, O. Bruhns, Choice of objective rate in single parameter hypoelastic deformation cycles, Computers & Structures 84 (17-18) (2006) 1134–1140.

[16] H. Xiao, O. Bruhns, A. Meyers, Hypo-elasticity model based upon the logarithmic stress rate, Journal of Elasticity 47 (1) (1997) 51–68.

[17] B. Bernstein, Hypo-elasticity and elasticity, Archive for Rational Mechanics and Analysis 6 (1) (1960) 89–104.

[18] B. Bernstein, Relations between hypo-elasticity and elasticity, Transactions of the Society of Rheology 4 (1) (1960) 23–28.

[19] J. Simo, On the computational significance of the intermediate configuration and hyperelastic stress relations in finite deformation elastoplasticity, Mechanics of Materials 4 (3-4) (1985) 439–451.

[20] J. Simo, M. Ortiz, A unified approach to finite deformation elastoplastic analysis based on the use of hyperelastic constitutive equations, Computer Methods in Applied Mechanics and Engineering 49 (2) (1985) 221–245.

[21] J. Löblein, J. Schröder, F. Gruttmann, Application of generalized measures to an orthotropic finite elasto-plasticity model, Computational Materials Science 28 (3-4) (2003) 696–703.

[22] C. Miehe, A formulation of finite elastoplasticity based on dual co-and contra-variant eigenvector triads normalized with respect to a plastic metric, Computer Methods in Applied Mechanics and Engineering 159 (3-4) (1998) 223–260.

[23] C. Miehe, N. Apel, M. Lambrecht, Anisotropic additive plasticity in the logarithmic strain space: modular kinematic formulation and implementation based on incremental minimization principles for standard materials, Computer Methods in Applied Mechanics and Engineering 191 (47-48) (2002) 5383–5425.

[24] P. Papadopoulos, J. Lu, A general framework for the numerical solution of problems in finite elasto-plasticity, Computer Methods in Applied Mechanics and Engineering 159 (1-2) (1998) 1–18.

[25] P. Papadopoulos, J. Lu, On the formulation and numerical solution of problems in anisotropic finite plasticity, Computer Methods in Applied Mechanics and Engineering 190 (37-38) (2001) 4889–4910.

[26] C. Sansour, W. Wagner, Viscoplasticity based on additive decomposition of logarithmic strain and unified constitutive equations: Theoretical and computational considerations with reference to shell applications, Computers & Structures 81 (15) (2003) 1583–1594.

[27] I. N. Vladimirov, M. P. Pietryga, S. Reese, Prediction of springback in sheet forming by a new finite strain model with nonlinear kinematic and isotropic hardening, Journal of Materials Processing Technology 209 (8) (2009) 4062–4075.

[28] I. N. Vladimirov, M. P. Pietryga, S. Reese, Anisotropic finite elastoplasticity with nonlinear kinematic and isotropic hardening and application to sheet metal forming, International Journal of Plasticity 26 (5) (2010) 659–687.

[29] M. Á. Caminero, F. J. Montáns, K. J. Bathe, Modeling large strain anisotropic elastoplasticity with logarithmic strain and stress measures, Computers and Structures 89 (11-12) (2011) 826–843.

[30] P. Neff, I.-D. Ghiba, Loss of ellipticity for non-coaxial plastic deformations in additive logarithmic finite strain plasticity, International Journal of Non-Linear Mechanics 81 (2016) 122–128.

[31] J. C. Simo, A framework for finite strain elastoplasticity based on maximum plastic dissipation and the multiplicative decomposition: Part i. continuum formulation, Computer Methods in Applied Mechanics and Engineering 66 (2) (1988) 199–219.

[32] J. C. Simo, A framework for finite strain elastoplasticity based on maximum plastic dissipation and the multiplicative decomposition. part ii: computational aspects, Computer Methods in Applied Mechanics and Engineering 68 (1) (1988) 1–31.

[33] J. C. Simo, Algorithms for static and dynamic multiplicative plasticity that preserve the classical return mapping schemes of the infinitesimal theory, Computer Methods in Applied Mechanics and Engineering 99 (1) (1992) 61–112.

[34] J. Simo, C. Miehe, Associative coupled thermoplasticity at finite strains: Formulation, numerical analysis and implementation, Computer Methods in Applied Mechanics and Engineering 98 (1) (1992) 41–104.

[35] A. L. Eterovic, K.-J. Bathe, A hyperelastic-based large strain elasto-plastic constitutive formulation with combined isotropic-kinematic hardening using the logarithmic stress and strain measures, International Journal for Numerical Methods in Engineering 30 (6) (1990) 1099–1114.

[36] G. Weber, L. Anand, Finite deformation constitutive equations and a time integration procedure for isotropic, hyperelastic-viscoplastic solids, Computer Methods in Applied Mechanics and Engineering 79 (2) (1990) 173–202.

[37] A. Cuitino, M. Ortiz, A material-independent method for extending stress update algorithms from small-strain plasticity to finite plasticity with multiplicative kinematics, Engineering Computations 9 (4) (1992) 437–451.

[38] G. Lührs, S. Hartmann, P. Haupt, On the numerical treatment of finite deformations in elastoviscoplasticity, Computer Methods in Applied Mechanics and Engineering 144 (1-2) (1997) 1–21.

[39] T. J. Grilo, I. N. Vladimirov, R. A. Valente, S. Reese, On the modelling of complex kinematic hardening and nonquadratic anisotropic yield criteria at finite strains: application to sheet metal forming, Computational Mechanics 57 (6) (2016) 931–946.

[40] A. Shutov, Efficient implicit integration for finite-strain viscoplasticity with a nested multiplicative split, Computer Methods in Applied Mechanics and Engineering 306 (2016) 151–174.

[41] C. Sansour, I. Karšaj, J. Sorić, On a numerical implementation of a formulation of anisotropic continuum elastoplasticity at finite strains, Journal of Computational Physics 227 (16) (2008) 7643–7663.

[42] C. Sansour, I. Karšaj, J. Sorić, A formulation of anisotropic continuum elastoplasticity at finite strains. part i: Modelling, International Journal of Plasticity 22 (12) (2006) 2346–2365.

[43] M. H. Ulz, A green–naghdi approach to finite anisotropic rate-independent and rate-dependent thermo-plasticity in logarithmic lagrangean strain–entropy space, Computer Methods in Applied Mechanics and Engineering 198 (41-44) (2009) 3262–3277.

[44] K. Bennett, R. Regueiro, D. Luscher, Anisotropic finite hyper-elastoplasticity of geomaterials with Drucker-Prager/Cap type constitutive model formulation, International Journal of Plasticity.

[45] H. Badreddine, K. Saanouni, A. Dogui, On non-associative anisotropic finite plasticity fully coupled with isotropic ductile damage for metal forming, International Journal of Plasticity 26 (11) (2010) 1541–1575.

[46] P. Neff, I.-D. Ghiba, Comparison of isotropic elasto-plastic models for the plastic metric tensor $C_p = F_p^T F_p$, in: Innovative Numerical Approaches for Multi-Field and Multi-Scale Problems, Springer, 2016, pp. 161–195.

[47] F. Aldakheel, P. Wriggers, C. Miehe, A modified Gurson-type plasticity model at finite strains: formulation, numerical analysis and phase-field coupling, Computational Mechanics 62 (4) (2018) 815–833.

[48] T. Brepols, I. N. Vladimirov, S. Reese, Application and evaluation of hyper-and hypoelastic-based plasticity models in the fe simulation of metal forming processes, PAMM 13 (1) (2013) 153–154.

[49] T. Brepols, I. N. Vladimirov, S. Reese, Numerical comparison of isotropic hypo- and hyperelastic-based plasticity models with application to industrial forming processes, International Journal of Plasticity 63 (2014) 18–48.

[50] M. Latorre, F. J. Montáns, Stress and strain mapping tensors and general work-conjugacy in large strain continuum mechanics, Applied Mathematical Modelling 40 (5-6) (2016) 3938–3950.

[51] M. Latorre, F. J. Montáns, Fully anisotropic finite strain viscoelasticity based on a reverse multiplicative decomposition and logarithmic strains, Computers & Structures 163 (2016) 56–70.

[52] M. Latorre, F. J. Montáns, Anisotropic finite strain viscoelasticity based on the sidoroff multiplicative decomposition and logarithmic strains, Computational Mechanics 56 (3) (2015) 503–531.

[53] M. Sanz, F. J. Montáns, M. Latorre, Computational anisotropic hardening multiplicative elastoplasticity based on the corrector elastic logarithmic strain rate, Computer Methods in Applied Mechanics and Engineering 320 (2017) 82–121.

[54] M. Zhang, F. J. Montáns, A simple formulation for large-strain cyclic hyperelasto-plasticity using elastic correctors. theory and algorithmic implementation, International Journal of Plasticity 113 (2019) 185–217.

[55] S. Reese, M. Pietryga, I. Vladimirov, Anisotropic finite plasticity based on structural tensorsdifferent strategies and application to forming simulations, International Journal of Material Forming 2 (1) (2009) 459.

[56] M. P. Pietryga, I. N. Vladimirov, S. Reese, On the use of explicit and implicit exponential map algorithms of finite strain combined hardening plasticity in the simulation of draw bending, in: Key Engineering Materials, Vol. 611, Trans Tech Publ, 2014, pp. 1796–1806.

[57] C. Jung-Ho, K. Noboru, An analysis of metal forming processes using large deformation elastic-plastic formulations, Computer Methods in Applied Mechanics and Engineering 49 (1) (1985) 71–108.

[58] K. Chung, S. Lee, F. Barlat, Y. Keum, J. Park, Finite element simulation of sheet forming based on a planar anisotropic strain-rate potential, International Journal of Plasticity 12 (1) (1996) 93–115.

[59] J. W. Yoon, D.-Y. Yang, K. Chung, F. Barlat, A general elasto-plastic finite element formulation based on incremental deformation theory for planar anisotropy and its application to sheet metal forming, International Journal of Plasticity 15 (1) (1999) 35–67.

[60] M. Saran, Comparison of elastic-plastic and rigid-plastic implicit fem simulations in sheet forming applications, Journal of Materials Processing Technology 27 (1-3) (1991) 279–300.

[61] J. Rojek, E. Onate, E. Postek, Application of explicit fe codes to simulation of sheet and bulk metal forming processes, Journal of Materials Processing Technology 80 (1998) 620–627.

[62] A. E. Tekkaya, State-of-the-art of simulation of sheet metal forming, Journal of Materials Processing Technology 103 (1) (2000) 14–22.

[63] M. Latorre, F. J. Montáns, On the interpretation of the logarithmic strain tensor in an arbitrary system of representation, International Journal of Solids and Structures 51 (7-8) (2014) 1507–1515.

[64] M. Miñano, M. A. Caminero, F. J. Montáns, On the numerical implementation of the closest point projection algorithm in anisotropic elasto-plasticity with nonlinear mixed hardening, Finite Elements in Analysis and Design 121 (2016) 1–17.

[65] M. Wali, H. Chouchene, L. Ben Said, F. Dammak, One-equation integration algorithm of a generalized quadratic yield function with Chaboche non-linear isotropic/kinematic hardening, International Journal of Mechanical Sciences 92 (2015) 223–232.

[66] J. M. Benítez, F. J. Montáns, The mechanical behavior of skin: Structures and models for the finite element analysis, Computers and Structures 190 (2017) 75–107.

[67] ADINA, Theory and Modeling Guide Volume 1: ADINA Solids and Structures, ADINA R&D (2017).

[68] P. Papadopoulos, J. Lu, On the formulation and numerical solution of problems in anisotropic finite plasticity, Computer Methods in Applied Mechanics and Engineering 190 (37-38) (2001) 4889–4910.

[69] C. Miehe, N. Apel, M. Lambrecht, Anisotropic additive plasticity in the logarithmic strain space: Modular kinematic formulation and implementation based on incremental minimization principles for standard materials, Computer Methods in Applied Mechanics and Engineering 191 (47-48) (2002) 5383–5425.

[70] R. Hill, A Theory of the Yielding and Plastic Flow of Anisotropic Metals, Proceedings of the Royal Society A: Mathematical, Physical and Engineering Sciences 193 (1033) (1948) 281–297.

[71] E. Voce, A practical strain hardening function, Metallurgia 51 (1955) 219–226.

[72] I. Vladimirov, S. Reese, Anisotropic finite plasticity with combined hardening and application to sheet metal forming, International Journal of Material Forming 1 (1) (2008) 293–296.

[73] F. Barlat, S. Panchanadeeswaran, O. Richmond, Earing in cup drawing face-centered cubic single crystals and polycrystals, Metallurgical Transactions A 22 (7) (1991) 1525–1534.

[74] J. W. Yoon, D. Y. Yang, K. Chung, F. Barlat, General elasto-plastic finite element formulation based on incremental deformation theory for planar anisotropy and its application to sheet metal forming, International Journal of Plasticity 15 (1) (1999) 35–67.

[75] J. W. Yoon, F. Barlat, R. E. Dick, K. Chung, T. J. Kang, Plane stress yield function for aluminum alloy sheets - Part II: FE formulation and its implementation, International Journal of Plasticity 20 (3) (2004) 495–522.

[76] NUMISHEET93, Benchmark Problem, in: A. Makinouchi, E. Nakamachi, E. Onate, R. Wagoner (Eds.), Proceedings of the 2nd International Conference on Numerical Simulation of Sheet Metal Forming Processes, Iseharay, Japan, 1993.

[77] NUMISHEET96, Benchmark Problem, in: J. Lee, G. Kitzel, R. Wagoner (Eds.), Proceedings of the 3rd International Conference on Numerical Simulation of Sheet Metal Forming Processes, The Ohio State University, USA, 1996.

[78] J. Kim, W. Lee, D. Kim, J. Kong, C. Kim, M. L. Wenner, K. Chung, Effect of hardening laws and yield function types on spring-back simulations of dual-phase steel automotive sheets, Metals and Materials International 12 (4) (2006) 293–305.

[79] J. Choi, J. Lee, G. Bae, F. Barlat, M. G. Lee, Evaluation of Springback for DP980 S Rail Using Anisotropic Hardening Models, The Journal of The Minerals, Metals & Materials Society 68 (7) (2016) 1850–1857.

[80] A. D. Anggono, W. A. Siswanto, Finite element simulation of deep drawing of steel-aluminium tailor-welded blanks, Proceedings of the 1st International Conference on Engineering Technology and Industrial Application.

[81] ADINA, Stamping of S-rail Part, `http://http://www.adina.com/stamping.shtml`, accessed: 2019-02-05.

[82] A. Makinouchi, Recent developments in sheet metal forming simulation, in: K.-i. Mori (Ed.), Simulation of Materials Processing. Theoty, Methods and Applications, Balkema, Lisse, 2001, pp. 3–15.